A ZCS/ZVS DC–DC Partial Power Converter With Reconfigurable H-Bridge and Variable Turns Ratio for an Integrated On-Board Charger

Niwton Gabriel Feliciani dos Santos, Jonatan Rafael Rakoski Zientarski, *Member, IEEE*, and Mário Lúcio da Silva Martins, *Member, IEEE*

***Abstract*—Series-connected partial power converters (S-PPCs) present the advantage of reduced losses due to part of the load power be delivered without any processing, i.e., losslessly. The remaining amount of processed power is required to offer load voltage or current regulation and it is subject of switching and conduction losses. Hence, the efficiency of an S-PPC is quite dependent on keeping its voltage regulation range (Δv) as narrow as possible. For electric vehicles battery chargers, Δv must cover from discharged to full charged traction battery pack voltage values, which often cover a wide voltage range and, thus, may minimize the benefits in employing S-PPC. To maintain the S-PPC advantages for such a wider voltage regulation range, this article proposes a step-up/down S-PPC with a reconfigurable H-bridge and variable turns ratio for the dc–dc stage of an integrated on-board charger (OBC). This way, Δv is split into multiple regions, covering from narrow to wider portions that allows the design of the S-PPC to be optimized for the narrow Δv during most of the constant current charging mode. This feature provides a significant efficiency improvement and it is achieved by using a tapped primary winding that allows the PWM switching pattern to be exchanged among the three primary-side H-bridge legs yielding in a set of three distinct transformer turns ratios specially designed to cover each region of Δv and reducing the current through the S-PPC. In addition, zero-current switching is achieved for the primary switches and zero-voltage switching for the secondary switches, which are ensured via two fixed-frequency modulation strategies, i.e., without any additional circuit component to suppress the high-voltage spikes across the primary switches. To validate the analyzes, a scale-down prototype was built for an OBC application example (2.2 kW), reaching a peak efficiency of 98.7% during charging.**

***Index Terms*—Integrated on-board charger (OBC), partial power processing (PPP), reconfigurable h-bridge.**

Manuscript received 18 March 2024; revised 4 June 2024; accepted 5 July 2024. Date of publication 12 July 2024; date of current version 4 September 2024. This work was supported in part by the Coordination for the Improvement of Higher Education Personnel – Brazil (CAPES/PROEX) – Finance Code 001, and in part by the National Institute of Science and Technology in Distributed Generation (INCT-GD) – CNPq processes under Grant 405054/2022-0, Grant 423405/2018-7, and Grant 308776/2018-6; CAPES under Grant 23038.000776/2017-54; and FAPERGS under Grant 17/2551-0000517-1. Recommended for publication by Associate Editor M. Narimani. *(Corresponding author: Niwton Gabriel Feliciani dos Santos.)*

Niwton Gabriel Feliciani dos Santos and Mário Lúcio da Silva Martins are with the Power Electronics and Control Research Group, Federal University of Santa Maria, Santa Maria, Rio Grande do Sul 97105-900, Brazil (e-mail: niwton.feliciani@acad.ufsm.br; mario-lucio.martins@ufsm.br).

Jonatan Rafael Rakoski Zientarski is with the Catarinense Federal Institute of Education, Science and Technology, Videira, Santa Catarina 89560-000, Brazil (e-mail: jonatan.zientarski@ifc.edu.br).

Color versions of one or more figures in this article are available at https://doi.org/10.1109/TPEL.2024.3426947.

Digital Object Identifier 10.1109/TPEL.2024.3426947

I. Introduction

THE transportation electrification employing battery-based electric vehicles (EVs) has become a clear tendency in order to reduce the consumption of fossil fuels and consequent greenhouse emissions [1]. The high-voltage traction battery pack of EVs is typically charged from a charging station (off-board) or from the utility ac grid via an on-board charger (OBC) [2]. According to the SAE J1772 standard, the charging power is limited to up to 1.92 kW (Level 1) when supplied by a standard convenience outlet [3]. The charging power can be increased to up to 19.2 kW (Level 2) with a dedicated EV supply equipment installed at home or public locations [3]. For Level 1 and Level 2, the OBC is connected to ac grid, meanwhile, for Level 3 chargers (above 19.2 kW) dc power supplies directly the battery pack [2] by means of an off-board charger. This off-board charge can handle high power levels (up to 350 kW) to charge the battery pack of the EVs in less than one hour [3]. To accomplish the adequate battery charging, conventional OBCs generally consist of a frontend power factor correction ac–dc converter followed by a dc–dc converter with the two sharing a common intermediate dc bus [4], [5], [6], as shown in Fig. 1(a). On the other hand, integrated OBCs have been developed by reusing the ac machine windings and the traction inverter as ac–dc stage, reducing their volume, weight and costs, [1], as shown in Fig. 1(b). To further reduce the OBC losses and ratings, the Type II configuration of S-PPC is proposed as the dc–dc stage [see Fig. 1(c)].

In EV charging applications, the battery pack voltage can vary in a wide operation range [4], which is challenging for the design and optimization of the power converters. In general, frequency-modulated LLC dc–dc converters are the prominent candidates [2], [6], [7] due to their characteristics, such as soft-switching operation, low electromagnetic interference (EMI), short-circuit protection capability, and also low components count [5], [7]. However, the variable switching frequency of LLC-based dc–dc converters vary in a quite wide range, which yields in a relatively low overall efficiency [8]. It also makes difficult to optimize the magnetics design in terms of volume and efficiency [5].

To restrict the frequency, duty cycle, or phase shift range and achieve a compromise between efficiency, power density, and output voltage range (VR), many reconfigurable topologies have been proposed for battery charging applications [8], [9],

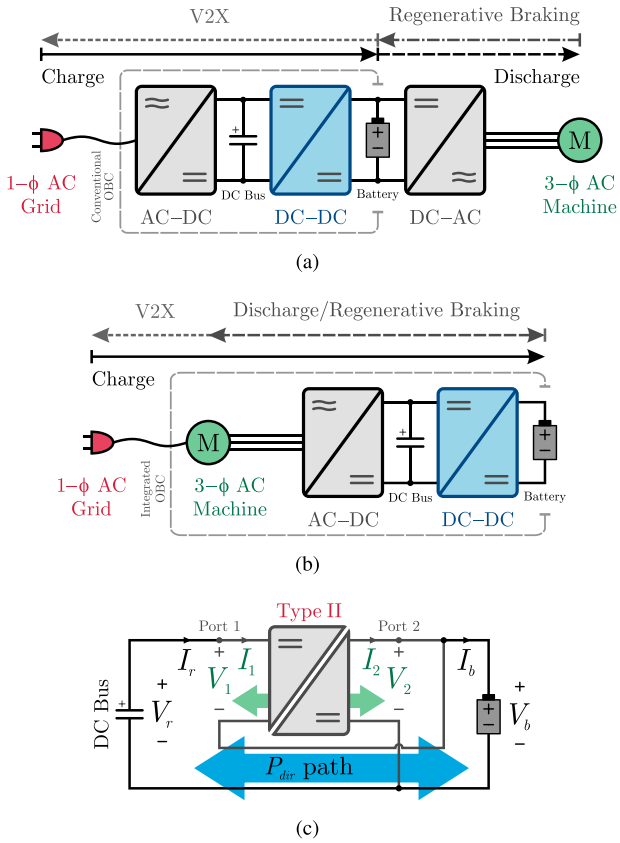

Fig. 1. System configuration of a (a) conventional and an (b) integrated single-phase OBC. (c) Type II configuration of a S-PPC.

[10], [11], [12], [13], [14], [15], where the use of different configurations enables optimizations to be performed for each one, thereby enhancing the performance throughout the entire charging process. In Wang et al.'s [8] work, an improved LLC converter using a reconfigurable transformer is proposed to charge a 250–450 V battery pack. In such a converter, the transformer can reconfigure its secondary side with two sets of turns ratios and tuned leakage inductances. A single-pole-double-throw relay is used to select the configurations, which is disadvantageous since relays typically have poor ON-state resistance properties and are slow, demonstrating a long transient regime. In Shu and Wang's [9] work, the output VR can be extended remarkably via three transformer turns ratios and a half-bridge configuration (conf.). In Lin's [10] work, an auxiliary switch is used to reconfigure the secondary side with two sets of turns ratios. The dc–dc converter includes an $LLCC$ circuit on the primary side and a reconfigurable push–pull circuit on the secondary side. In Shahzad et al.'s [11] work, a half-bridge $2LLC$ resonant converter with two configurations is proposed to extend the output VR. In short, the hybrid rectifier on the secondary side can be reconfigured as a bridge rectifier or a voltage doubler.

The partial power processing (PPP) concept has attracted much attention recently [16], [17] and can be considered for EV charging applications. However, the application in OBCs has not been fully investigated, and few studies have been published in the top quality power electronics publications [18]. Recent relevant papers mainly focus on the application in fast charging stations (FCSs) [19], [20]. The concept of PPP relies on the idea that a PPP converter (PPC) processes only a fraction of the total active power supplied to the system [17]. In case of the series-connected PPCs (S-PPCs), they regulate the voltage difference between the input and output of the system (they are arranged as a buffer in series with the input/output), and their benefits, such as the reduction of losses, are fully achieved only if the voltage gain range, duty cycle, and turns ratio are well designed [16]. Their configuration is usually Type I or II [14], where the Type I connections resemble those of an input-parallel–output-series architecture and the Type II connections resemble those of an input-series–output-parallel architecture [18]. Although, some S-PPCs in the literature can be reconfigured as Type I or Type II [14]. Compared to step-up and step-down S-PPCs, the use of voltage step-up/down S-PPCs culminates in a further reduction of the active and nonactive power processed, further reducing component stresses, converter losses, and size.

According to dos Santos et al.'s [16] work, the Type II configuration shown in Fig. 1(c) is more suitable for use in step-down systems or in step-up/down systems where the input voltage is fixed, as in the typical case of the dc–dc stage of OBCs [5]. In this case, a boost-type current-fed (CF) isolated converter needs to be selected as the step-down or step-up/down S-PPC. In such converters, unfortunately, the current mismatching between the leakage and input currents usually introduces high-voltage spikes across the switches on the primary side at their turn-OFF, which can increase the EMI, reduce the system reliability, and further damage those expensive devices [21]. Wherefore, passive snubbers or active-clamp circuits are generally used to mitigate the voltage spikes, reduce oscillations, and assist in soft-switching [22], [23]. However, additional hardware has a negative impact on the efficiency, volume, and costs. Therefore, modulation-oriented approaches are preferred in case of the CF converters, including natural commutation techniques that achieve soft-switching without auxiliary circuits [24], [25].

In order to overcome all the challenges associated with OBCs and achieve a good compromise between power processing, efficiency, and battery VR, this article proposes a Type II S-PPC with a reconfigurable H-bridge for the dc–dc stage of an integrated OBC. The concepts of S-PPCs and reconfigurable converters are not new; however, their combined application remains unexplored in the literature, particularly in the field of battery-based EVs [14]. With the reconfigurable H-bridge implemented in the proposed S-PPC, it can reconfigure its transformer primary side with three (3) sets of turns ratios, which are designed to cope with a wide voltage regulation range (Δv) and extend it only when necessary, reducing the conversion effort on the converter (reducing conduction losses) by minimizing the circulating currents. With an appropriate design, the proposed S-PPC can operate predominantly within a VR where the turns ratio is higher and the circulating currents are lower in comparison with the S-PPC based on a nonreconfigurable H-bridge. The additional advantages of the proposed reconfigurable S-PPC are summarized as follows.

1) The variable turns ratio approach allows the S-PPC to operate in a wide VR with high performance. Equally important, it is bidirectional and has the capability to step up or step down the voltage in both directions of power flow (the dc bus voltage during charging and the battery pack voltage during the discharging mode). In this case, a design procedure to select the turns ratios and leakage inductances is proposed in this article.
2) The proposed S-PPC has an inductor connection on both the input and output terminals of the dc–dc stage. Hence, nonpulsating current with low high-frequency (HF) ripple can be achieved on both sides of such a stage [21].
3) A full-range zero-current switching (ZCS) is achieved for the switches on the primary side, while zero-voltage switching (ZVS) is achieved for the secondary switches. The soft-switching operation in step-down and step-up modes is ensured with two modulation-oriented approaches proposed here.
4) These two modulation-oriented approaches are actually pulsewidth modulation (PWM) strategies. The fixed-frequency operation makes it easy to optimize the magnetics design [25] and simplifies the control implementation [24].
5) Finally, any passive snubber and/or active-clamp circuit is employed to suppress the high turn-OFF voltage spikes across the primary switches, being the absence of snubbers an advantage, since one of the major reasons for efficiency degradation is the presence of snubber losses [24], [25]. In addition, the proposed S-PPC does not require any additional relays or contactors for reconfiguration.

II. Steady-State Analysis of the Proposed S-PPC

In this section, the proposed current-fed full-bridge/output-series half-bridge (CFFB/OSHB) Type II S-PPC is put forward and its steady-state behavior for continuous conduction mode is described in detail. Here, three assumptions are made in order to simplify the evaluation of the proposed S-PPC in the following.

1) The switching and energy-storage devices are ideal and lossless.
2) The capacitors are large enough to consider their voltages constant during one switching period.
3) The transformer is modeled with a magnetizing inductance (L_M) and a leakage inductance (L_k) referred to the primary side. However, L_M is assumed to be large enough to consider its current as null.

A. Step-Up/Down Type II S-PPC Topology Derivation

Fig. 2 illustrates the different circuits that can be used to implement the current-ripple-friendly ports of the proposed bidirectional step-up/down Type II S-PPC system. In such a case, the port 1 of the isolated dc–dc converter [see Fig. 1(c)] comprises the CF full-bridge [see Fig. 2(a)], half-bridge [see Fig. 2(b)], and push–pull [see Fig. 2(c)] reconfigurable circuits. Meanwhile, the port 2 comprises the CF full-bridge [see Fig. 2(d)], symmetrical half-bridge [see Fig. 2(e)], and asymmetrical half-bridge [see Fig. 2(f)] voltage clamped circuits, where the transformer winding voltage is clamped with the capacitors, mitigating any voltage spike across the switches, as in voltage-fed (VF) ports [21].

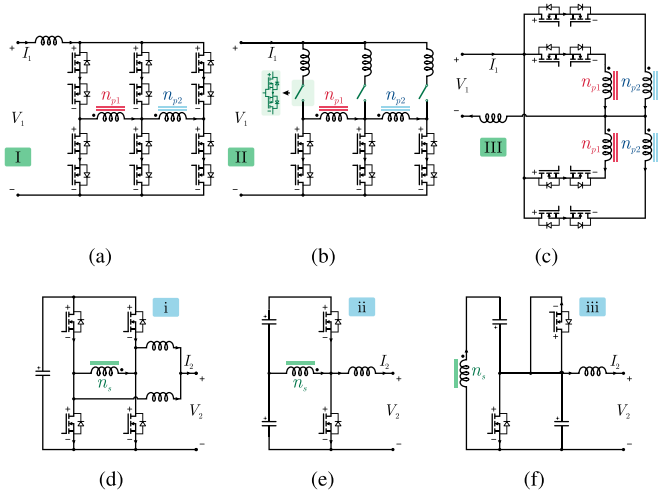

Fig. 2. Design examples of possible circuits for the current-ripple-friendly ports of the proposed step-up/down Type II S-PPC system. Possible circuits for (a)–(c) port 1 (reconfigurable) and (d)–(f) port 2.

TABLE I
Characteristics of the Type II S-PPCs Derived From Fig. 2

Combination	S	C	L	T_w	Confs.	ξ
I−i	16	1	3	3	3	7.7
I−ii	14	2	2	3	3	7.0
I−iii	14	2	2	3	3	7.0
II−i	16	1	5	3	3	8.3
II−ii	14	2	4	3	3	7.7
II−iii	14	2	4	3	3	7.7
III−i	12	1	3	5	2	10.5
III−ii	10	2	2	5	2	9.50
III−iii	10	2	2	5	2	9.50

The main characteristics of the Type II S-PPCs derived from the combination of the circuits shown in Fig. 2 are listed in Table I. These characteristics are the number of switches (S), capacitors (C), inductors (L), transformer windings (T_w), as well as the number of possible configurations (NoC). Based on these values, the following quantitative factor (ξ) has been employed to evaluate the combinations:

$$\xi = \frac{S + C + L + T_w}{\text{NoC}} \tag{1}$$

which indicates that having many components or few possible confs. results in a high factor, which is disadvantageous.

As can be seen in Table I, combinations III−i, III−ii, and III−iii exhibit the worst characteristic in terms of ξ (despite employing fewer switches), while combinations II−i, II−ii, and II−iii exhibit middling characteristics similar to I−i. Therefore,

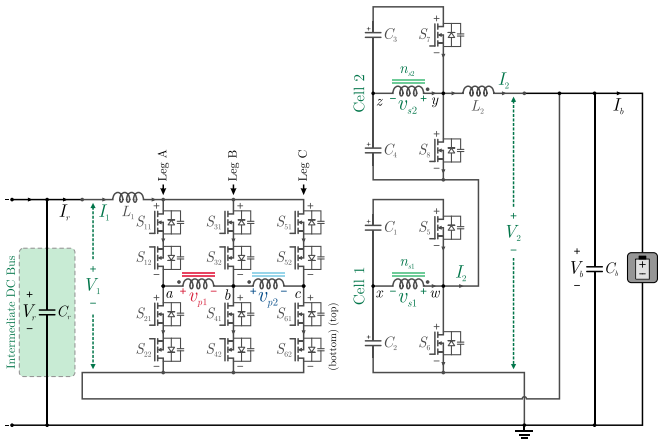

Fig. 3. Proposed step-up/down CFFB/OSHB S-PPC.

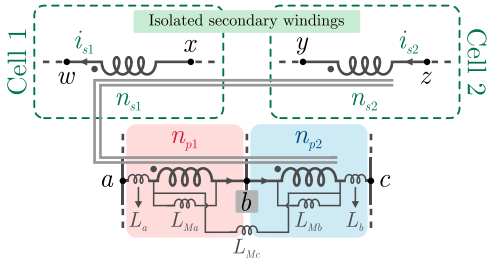

Fig. 4. Reconfigurable transformer of the proposed CFFB/OSHB S-PPC.

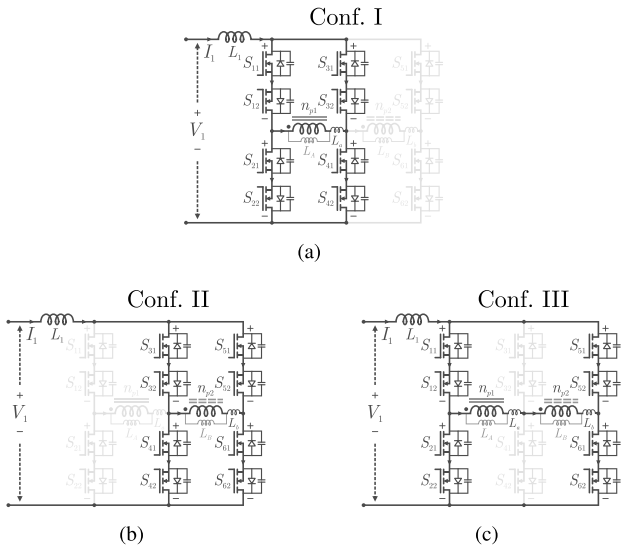

Fig. 5. Different configurations of the CFFB equivalent circuit. (a) Conf. I (legs A and B). (b) Conf. II (legs B and C). (c) Conf. III (legs A and C).

the S-PPCs derived from combinations I−ii and I−iii are the ones that offer more benefits than the others, i.e., are the best balance approaches for the proposed application.

B. Proposed Step-Up/Down Type II S-PPC Description

Fig. 3 shows the topology of the step-up/down CFFB/OSHB S-PPC, which is derived from combination I−ii. As shown, it is composed of six four-quadrant switches (S_{1x}−S_{6x}) on the primary side (CFFB circuit), four two-quadrant switches (S_5−S_8) on the secondary side (OSHB circuit), two inductors (L_1 and L_2), and six capacitors (a dc bus capacitor C_r, an output capacitor C_b, and C_1−C_4). Here, V_r and V_b are the dc bus and battery voltages, as well as I_r and I_b are the dc bus and battery currents, respectively. Finally, V_i and I_i are used to denote the voltage and current of port i ($i = 1, 2$).

A high-current ripple has a negative impact on the battery management system, performance, and lifetime of the EVs lithium-ion batteries [21]. Therefore, limiting the battery current ripple is quite important. As mentioned in Section I, the CFFB/OSHB S-PPC has an inductor connection on both the ports 1 and 2, which is possible because it presents two middle section capacitive buffers (C_1−C_2 in cell 1 and C_3−C_4 in cell 2) connected to the secondary side current section [26]. Hence, nonpulsating current with low HF ripple can be achieved on both sides of the dc–dc stage. The use of two stacked half-bridge cells at port 2 is made to reduce the maximum voltages across the switches.

The CFFB and OSHB equivalent circuits are coupled with a reconfigurable transformer composed of a HF transformer with a tapped primary winding and two separated secondary windings, as illustrated in Fig. 4. This transformer provides the functional isolation required for the system to function properly, but the dc bus and the battery pack are grounded to the same reference. Since the high-voltage battery pack is generally not grounded to the chassis of an EV for safety reasons, the proposed integrated OBC satisfies the SAE J1772 standard for conductive chargers [27]. It refers to the system grounding; however, the battery pack enclosure is also generally not grounded to the chassis (equipment grounding). Hence, the prevention of potential electrical hazards is ensured in normal scenarios, also culminating in a reduction of the risk of electric shock in the event of a collision.

C. Operation Principles

1) Reconfigurable H-Bridge: In the S-PPC, the use of four-quadrant switches on the primary side serves for two purposes: i) to operate within a bipolar voltage regulation range at port 1 (thereby narrowing Δv); and ii) to select the appropriate VR from a set of narrow ranges and change it when necessary. This is achieved by controlling the ON/OFF states of the switches of legs A–C; S_{11}−S_{61} in step-down and S_{12}−S_{62} in step-up modes. Here, two active switches are arranged back-to-back to form each four-quadrant switch [28].

Fig. 5 shows the three configurations of the CFFB equivalent circuit. In short, conf. I is activated when leg C is disabled for the entire switching period (T_S) and the CFFB is operated by modulating the four-quadrant switches S_{1x}−S_{4x}, as shown in Fig. 5(a). The switching frequency is given by $f_s = 1/T_S$. Analogously, conf. II is activated when leg A is disabled and the CFFB is operated by modulating S_{3x}−S_{6x}, as shown in Fig. 5(b). Finally, conf. III is activated when leg B is disabled

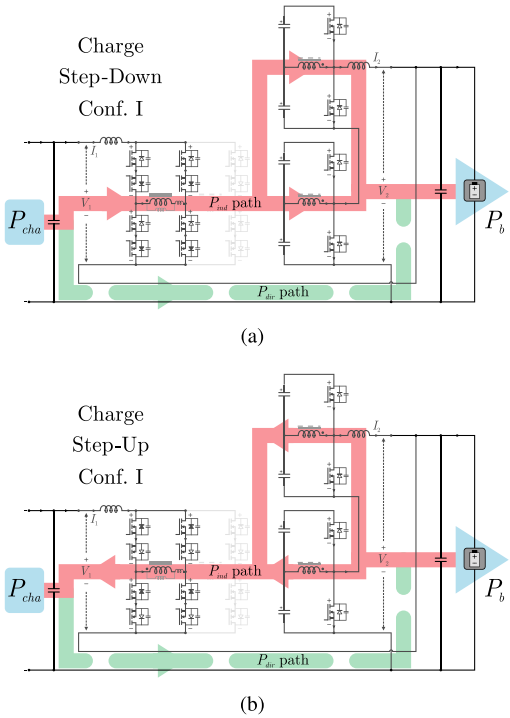

Fig. 6. Power flow between the ports of the proposed S-PPC during charging (using conf. I as an example). (a) Step-down. (b) Step-up modes.

and the CFFB is operated by controlling the other switches on the primary side, as shown in Fig. 5(c).

Due to the reconfiguration, the transformer has three turns ratios (n), magnetizing inductances, and leakage inductances

$$n = n_a = \frac{n_{sx}}{n_{p1}},\ L_M = L_{Ma},\ L_k = L_a, \quad \text{in Conf. I}$$
$$n = n_b = \frac{n_{sx}}{n_{p2}},\ L_M = L_{Mb},\ L_k = L_b, \quad \text{in Conf. II}$$
$$n = n_c = \frac{n_{sx}}{n_{pc}},\ L_M = L_{Mc},\ L_k = L_c, \quad \text{in Conf. III} \tag{2}$$

where $n_{sx} = n_{s1} = n_{s2}$, $n_{pc} = n_{p1} + n_{p2}$, and $L_c \approx L_a + L_b$. Accordingly, v_{ph} and v_{sx} are the voltages across the primary (including the leakage inductance) and secondary sides (for $h = 1, 2$), respectively. The equivalent primary voltage presents three levels in each conf. ($-\frac{V_2}{2n}$, 0, and $+\frac{V_2}{2n}$), and the secondary voltage presents only two levels ($-V_2$ and $+V_2$).

Therefore, by adopting the reconfigurable H-bridge approach, there is a design degree of freedom in customizing the turns ratios and tune the leakage inductances of the transformer, which can be designed to reduce the nonactive power processed [16]. Since this reduces the nonactive power losses by reducing the circulating currents, the efficiency can be improved.

2) Step-Up/down Conversion Ratio: Fig. 6 shows the power flow between the ports of the CFFB/OSHB S-PPC during charging (using conf. I as an example). During the charging mode of the EV battery pack, the charging power (P_{cha}) is transferred from the intermediate dc bus to the battery pack. In this case, the charging power flows through two paths [16]. The amount that flows through the bottom path represents the direct power (P_{dir}), which is directly transferred from the dc bus to the battery pack without being processed, which means that this path is highly efficient ($\eta \approx 1$ [18]). On the contrary, the amount flowing through the top path represents the indirect power (P_{ind}), which is processed by the circuit devices and yields in power losses. Therefore, it can be written that

$$P_{\text{cha}} = P_{\text{dir}} + P_{\text{ind}}$$
$$V_r I_r = V_2 I_1 + V_1 I_1$$
$$V_b I_b = V_2 I_1 + V_2 I_2 \tag{3}$$

in case of an ideal lossless S-PPC, where $P_{\text{cha}} = P_b$.

As can be seen, the P_{cha} and P_{dir} paths are unidirectional. Conversely, the indirect power flows in both directions, which occurs because the CFFB/OSHB S-PPC operates with bipolar voltage at port 1 and bidirectional current at port 2. Hence, the proposed integrated OBC system operates in step-down ($P_{\text{ind}} > 0$) and step-up modes ($P_{\text{ind}} < 0$). These two modes with different voltage gain ranges are selected based on the actual battery pack voltage value. Table II presents a summary regarding the voltage polarity and current direction at ports 1 and 2 during the charging mode.

TABLE II
VOLTAGE, CURRENT, AND POWER FLOW: PORTS 1 AND 2

Variable	Equation	Step-down mode	Step-up mode
V_1	$V_r - V_b$	positive (+)	negative (−)
V_2	V_b	positive (+)	positive (+)
I_1	I_r	positive (+)	positive (+)
I_2	$I_b - I_r$	positive (+)	negative (−)
P_{ind}	$P_{\text{cha}} - P_{\text{dir}}$	port 1 to 2	port 2 to 1

The detailed operation of the CFFB/OSHB Type II S-PPC in step-down and step-up modes (during charging) is explained in the following. During the discharging mode, the system active power is transferred from the battery pack to the dc bus [see Fig. 1(b)], but the operation is similar to that during charging.

Step-down mode: When $V_r > V_b$, the proposed CFFB/OSHB S-PPC operates in step-down mode, where $V_1 > 0$ and $I_2 > 0$. In conf. I, for instance, the bottom switches of S_{1x}–S_{4x} (S_{12}–S_{42}) are ON for the entire switching period, while the PWM strategy is applied to the top switches (S_{11}–S_{41}). The diagonal switch pairs of the CFFB equivalent circuit (S_{11}, S_{41} and S_{21}, S_{31}) are operated with identical gating signals phase-shifted by 180° with an overlap. On the secondary side, the switches operate with a fixed duty cycle of 0.5 pu. The gating signals of S_5 and S_7 are the same, as well as the gating signals of S_6 and S_8, and these two signals are complementary to each other. The operation in conf. II and conf. III is similar to that in conf. I.

The key waveforms of the proposed CFFB/OSHB S-PPC operating in step-down mode (using conf. I as an example) are illustrated in Fig. 7. Omitting the dead time intervals, the S-PPC presents six operating circuit stages (①–⑥), where the relation between the PWM duty cycle (d_p), overlapping duty cycle (d_v),

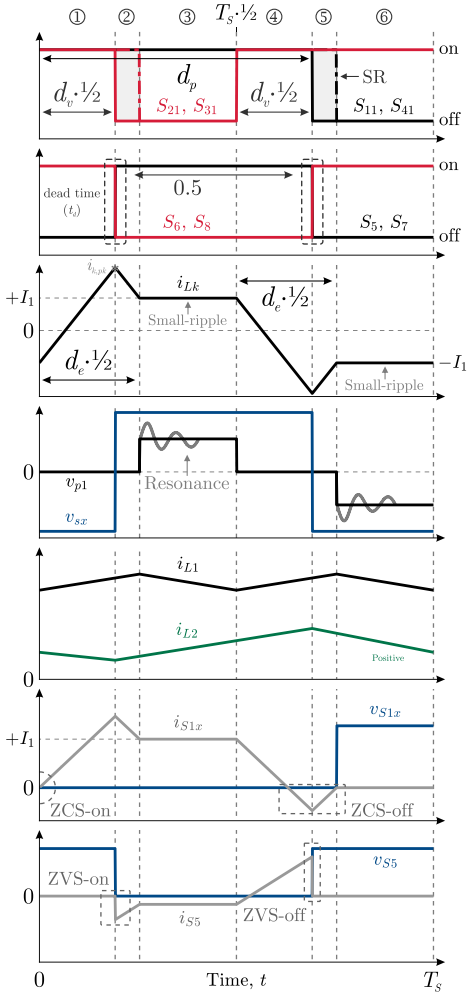

Fig. 7. Steady-state waveforms of the proposed step-up/down CFFB/OSHB S-PPC in step-down mode (using conf. I as an example).

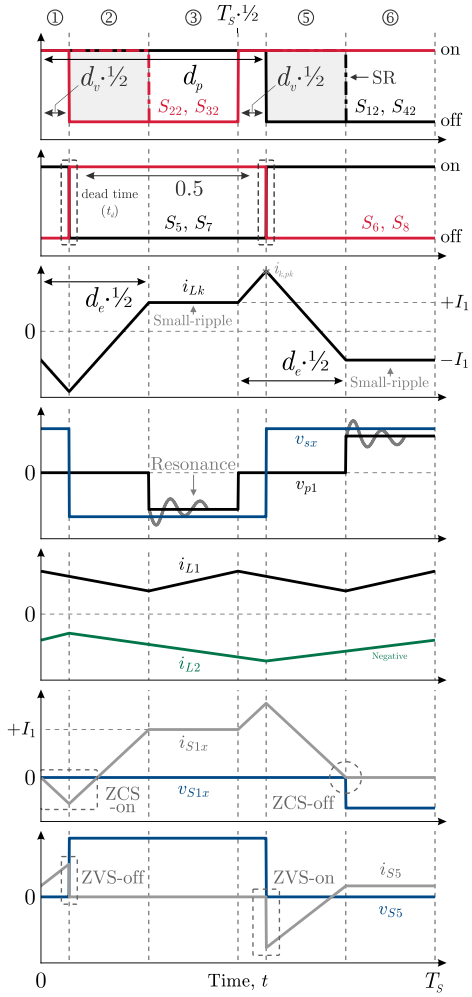

Fig. 8. Steady-state waveforms of the proposed step-up/down CFFB/OSHB S-PPC in step-up mode (using conf. I as an example).

and actual duty cycle (d_e) is given by

$$d_p = \frac{(1+d_v)}{2}, \quad d_e = d_v + \delta, \quad \delta = d_v - \frac{8n\varpi}{M_C} \tag{4}$$

where ϖ is the normalized leakage inductance defined in (17) and $M_C = V_2/V_1$. Considering the continuous loop and the voltage balance of L_1, d_p and d_e can vary between 0.5–1 and 0–1, respectively. If $\delta \approx 0, \therefore d_e \approx d_v$.

In Figs. 7 and 8, v_{S1x} and i_{S1x} are the instantaneous voltage and current of S_{1x}, v_{S5} and i_{S5} are the voltage and current of S_5, and i_{Lk} is the instantaneous leakage current. The primary switches present similar operation waveforms, as well as the switches S_5–S_8. In addition, "–·–" in the very top waveforms represent the increment by which the pulse width of the gate–source signals (v_{gS}) of the primary switches must be increased for the implementation of the synchronous rectification (SR). It helps in reducing conduction losses by preventing current from flowing through the body diodes [29].

In this mode, the peak value of i_{Lk} is given by

$$i_{k,pk} = I_1 \left(\frac{d_v M_C}{4\, n\, \varpi} - 1 \right). \tag{5}$$

As a result of the proper operation of the S-PPC with the proposed PWM strategy shown in Fig. 7, ZCS turn-ON and turn-OFF are naturally achieved for all the switches on the primary side. The switches S_{11}–S_{61} turn-OFF with ZCS owing to the conduction of their body diodes (or their conductive channel with the SR [29]) and turn-ON with ZCS due to the low rise rate of the turn-ON currents (di/dt) [30]. In addition, the dead time (t_d) between the secondary switches on the same cell provides ZVS turn-ON for S_5–S_8 owing to the reverse current (conduction of their body diodes) generated to discharge their output capacitances (C_{oss}) before the switches are turned ON. These four switches are also turned OFF with ZVS, which occurs due to the low rise rate of the turn-OFF voltages (dv/dt) [30].

In summary, the key condition for achieving the true ZVS turn-ON and true ZCS turn-OFF operations is the reverse current generated before the switches are turned ON or OFF, respectively. On the other hand, the ZVS-OFF and ZCS-ON are not real soft-switching forms and only occur by employing snubber capacitors (or the output capacitances) to limit the rise rate of the turn-OFF voltages (false ZVS turn-OFF), or small inductors to limit the rise rate of the turn-ON currents (false ZCS

turn-ON) [30]. In this article, the snubber capacitors are not used, and the small inductors are composed of the intrinsic leakage inductances of the transformer and two series inductors.

Step-up mode: When $V_r < V_b$, the S-PPC operates in step-up mode, where $V_1 < 0$ and $I_2 < 0$. In conf. I, for instance, the top switches of $S_{1x}-S_{4x}$ ($S_{11}-S_{41}$) are ON for the entire period T_S, while the PWM strategy is applied to the bottom switches ($S_{12}-S_{42}$). As in step-down mode, the diagonal switch pairs are operated with identical gating signals phase-shifted by 180°. On the secondary side, the switches operate almost the same as in step-down mode. The gating signals of S_5 and S_7 are still the same, as well as the gating signals of S_6 and S_8; however, the ON/OFF states of these two-quadrant switches are inverted in relation to those in that mode.

In this mode, the true ZVS turn-ON and false ZVS turn-OFF are also achieved for all the two-quadrant switches on the secondary side of the CFFB/OSHB S-PPC. Furthermore, the true ZCS turn-OFF and false ZCS turn-ON are also naturally achieved for all the switches on the primary side. Consequently, the proposed S-PPC can reduce or almost eliminate all the switching losses [30], enabling operation at higher switching frequencies to improve power density [12].

The key waveforms of the proposed CFFB/OSHB S-PPC operating in step-up mode (using conf. I as an example) are illustrated in Fig. 8, where $d_e = d_v + \delta$. Here, however

$$\delta = d_v + \frac{8n\varpi}{M_C}, \qquad i_{k,pk} = I_1\left(\frac{d_v M_C}{4\,n\,\varpi} + 1\right). \tag{6}$$

3) Soft-Switching Conditions: In step-down mode, when one diagonal switch pair of the CFFB equivalent circuit turns OFF, there could be two types of voltage components across the primary switches: voltage oscillation (v_{osc}) and voltage spike (v_{spk}). The primary switches achieve ZCS turn-OFF operation *only if* $i_{Lk} \geq +I_1$ (assuming small-ripple approximation [28]) at the end of stage ① and $i_{Lk} \leq -I_1$ at the end of stage ④, causing the required reverse current to flow through their body diodes or conductive channels before the turn-OFF moment. Thus, to ensure ZCS-OFF for $S_{11}-S_{61}$ in step-down mode

$$|\pm i_{k,pk}| \geq |\pm I_1|, \qquad \text{resulting in } v_{\text{spk}} = 0 \tag{7}$$

i.e., this condition naturally ensures the high turn-OFF voltage spike suppression of the switches without any passive snubber and/or active-clamp circuit (commonly used in conventional CF converters [24]), because the soft-switching effectively absorbs all the energy accumulated in the leakage inductance in this case. The condition also ensures false ZCS-ON for $S_{11}-S_{61}$.

By manipulating the expressions in (5) and (7), one can find the ZCS condition as a function of L_k

$$L_k \leq L_{\text{cr}}, \qquad \text{where} \quad L_{\text{cr}} = \frac{M_C d_v V_1}{8 n f_s I_1}. \tag{8}$$

Fig. 9(a) illustrates all the three attainable leakage current waveforms (in function of L_k) during the switching transition of $S_{11}-S_{61}$ from stage ① to ③, in case of the step-down mode. Basically, if the ZCS condition in (8) is not satisfied, the current mismatching between i_{Lk} and I_1 will cause a high rise rate in the leakage current during the transition, which will introduce high-voltage spikes across the primary switches. In this case, the amplitude of v_{spk} can reach thousands of volts

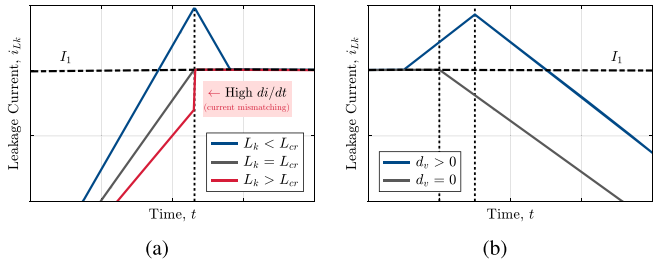

Fig. 9. Leakage current waveforms during the switching of $S_{1x}-S_{6x}$: (a) Step-down and (b) step-up modes, in function of L_k and d_v, respectively.

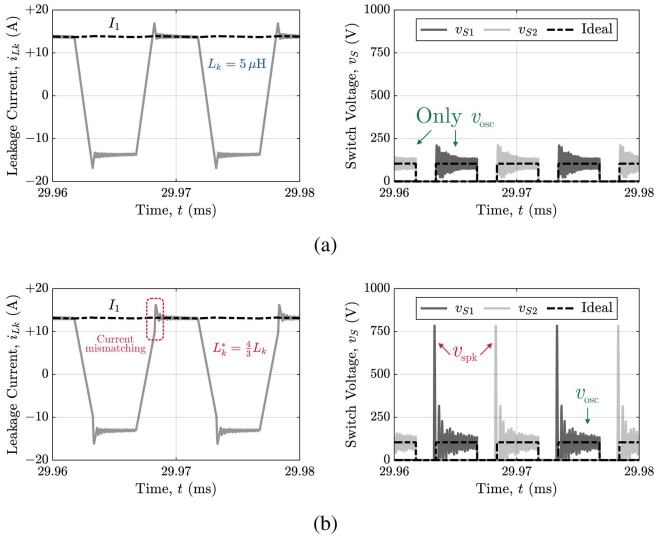

Fig. 10. Simulation waveforms of the leakage current and voltage across the switches $S_{1x}-S_{2x}$ in step-down mode (using conf. I as an example). (a) Complete ($L_k < L_{\text{cr}}$). (b) Incomplete ($L_k > L_{\text{cr}}$) ZCS transitions.

and damage the switches, reducing the system reliability. For example, by considering an ON-resistance (R_{on}) of 64 mΩ and a C_{oss} of 70 pF for the primary switches, Fig. 10 shows the simulation waveforms of the leakage current and voltage across the switches $S_{1x}-S_{2x}$ in step-down mode (using conf. I as an example); Fig. 10(a) for a complete ZCS transition with the voltage spike suppression and Fig. 10(b) for an incomplete ZCS transition ($L_k > L_{\text{cr}}$) where $v_{\text{spk}} > 750$ V.

In general, the value of L_k is practically constant, while the duty cycle varies according to the voltage gain variation. Thus, for a given L_k, the ZCS condition needs to be rewritten as

$$d_v \geq \frac{8n\varpi}{M_C} \tag{9}$$

which is mandatory for the proper operation of the S-PPC with the proposed PWM strategy shown in Fig. 7.

To ensure ZCS for $S_{12}-S_{62}$ in step-up mode, there are no necessary conditions. Indeed, only the following restrictions need to be satisfied: $L_k \geq 0$ and $d_v \geq 0$. Fig. 9(b) illustrates the two attainable leakage current waveforms (in function of d_v) during the switching transition of $S_{12}-S_{62}$ from stage ③ to ⑤, in step-up mode. Here, there are no operation conditions that culminate in the current mismatching between i_{Lk} and I_1

during the transition, because i_{Lk} is always equal to or greater than I_1 at these moments. Hence, the high-voltage spikes across the primary switches are naturally avoided.

Since the proposed CFFB/OSHB S-PPC is snubberless, the voltage oscillation cannot be eliminated in both the step-down and step-up modes. The oscillation energy is related to the 1) leakage inductance and the 2) equivalent capacitance (C_{eq}) that includes both the parasitic capacitances of the transformer and the output capacitance of the switches. In short, the amplitude of v_{osc} is calculated as follows:

$$v_{\text{osc}} = V_1\,[1 - \cos(\omega t)] \pm V_2/(2n) \tag{10}$$

where "±" is "+" in step-down mode and is "−" in step-up mode, and ω is the time constant given by

$$\omega = 1/\sqrt{L_k\, C_{\text{eq}}}. \tag{11}$$

Regarding the two-quadrant switches on the secondary side of the CFFB/OSHB S-PPC, S_5 and S_7 achieve ZVS turn-ON operation only if the following condition is satisfied [31]:

$$+i_{k,pk} \geq +2\,n\,i_{2,n} \begin{cases} \text{at the end of } ① \text{ (step-down)} \\ \text{at the end of } ④ \text{ (step-up).} \end{cases} \tag{12}$$

Similarly, S_6 and S_8 achieve ZVS turn-ON only if

$$-i_{k,pk} \leq +2\,n\,i_{2,p} \begin{cases} \text{at the end of } ④ \text{ (step-down)} \\ \text{at the end of } ① \text{ (step-up).} \end{cases} \tag{13}$$

In (12) and (13), $i_{2,n}$ and $i_{2,p}$ are defined as

$$i_{2,n} = I_2 - \Delta i_{L2}/2, \quad i_{2,p} = I_2 + \Delta i_{L2}/2 \tag{14}$$

where Δi_{L2} is the current ripple of the inductor at port 2.

In order to ensure enough time for discharging the output capacitances of the secondary switches before they are turned ON, the dead time between the switches on the same half-bridge cell must comply with the following constraint:

$$t_d \leq \frac{T_S}{2}\left[d_v \pm \frac{-4n\varpi(M_C + 2n)}{M_C^2}\right]. \tag{15}$$

As long as the values of C_{oss} are sufficient, the condition in (15) also ensures ZVS-OFF for the secondary switches.

4) Static Voltage Gain: By applying the principle of inductor volt–second balance [28] to the dc bus inductor (L_1), through which flows a current whose average value is $I_{L1} = I_1$, the voltage gain V_2/V_1 can be derived as shown in (16) shown at the bottom of this page, where

$$\varpi = \frac{L_k\, f_s}{R_1}, \quad \varphi = \frac{L_1\, f_s}{R_1}, \quad \kappa = \frac{L_k}{L_1}, \quad R_1 = \frac{V_1}{I_1} \tag{17}$$

where φ is the normalized dc bus filter inductance, κ is the ratio of inductances, and R_1 is the resistance of port 1.

In (16), "±" is also "+" in step-down and "−" in step-up modes, where M_C varies from positive to negative gains via the energy stored in the passive filters. Due to the inherent boost function between ports 1 and 2, $|M_C| \geq 1$.

The voltage gain of the dc–dc stage (M) is given by

$$M = \frac{V_b}{V_r} = \frac{I_r}{I_b} = \frac{M_C}{1 + M_C}. \tag{18}$$

It is worth mentioning that the magnetization/demagnetization of the port 2 inductor (L_2) does not affect M_C and M. The average value of the current through L_2 is $I_{L2} = I_2$.

By considering the battery pack VR defined later in Section III, Fig. 11(a) shows the voltage gain variation of the CFFB/OSHB S-PPC for arbitrary values of n (for $L_1 = 500\,\mu$H and $\kappa = 0.01$), considering only one conf. of the CFFB circuit (such as a traditional nonreconfigurable H-bridge) and the proposed H-bridge reconfiguration. On the other hand, Fig. 11(b) shows the voltage gain variation for different values of κ (for $L_1 = 500\,\mu$H and $n = 1.30$). For the same values of n and L_k, varying only the inductance of L_1 has little effect on the static voltage gain and operation of the S-PPC.

In Fig. 11(a) and (b), the light red shaded areas represent the inoperable regions where the voltage regulation is lost due to the incomplete ZCS transition, i.e., where the overlapping duty cycle does not comply with the constraint in (9). Accordingly, the proper design of the turns ratios and leakage inductances of the proposed reconfigurable S-PPC must ensure operation with ZCS throughout the entire battery pack VR, in both the step-down ($M < 1$) and step-up ($M > 1$) modes.

Fig. 11(c) shows the theoretical and circuit simulation results referring to the voltage gain of the proposed reconfigurable S-PPC, considering the same values of n as in Fig. 11(a) and the VR of the constant current (CC) mode defined later in Section III. In this figure, the lines correspond to the numerical solution of (16) and (18), and the markers correspond to some data points from the circuit simulation. As can be seen, the data points are compatible with the numerical solution.

5) Voltage Stresses: Ideally, the OFF-state voltage of the primary switches S_{1x}–S_{6x} ($V_{pS,\max}$) and secondary switches S_5–S_8 ($V_{sS,\max}$), and the average voltage of the capacitors C_1–C_4 of the CFFB/OSHB S-PPC are given by

$$V_{pS,\max} = \pm V_2/(2n), \quad V_{sS,\max} = V_2, \quad V_{C14} = V_2/2. \tag{19}$$

However, the maximum value of v_{osc} in (10) implies that

$$V_{pS,\max} = 2V_1 \pm V_2/(2n) \tag{20}$$

which will only occur when $\cos(\omega t)$ in (10) is equal to -1.

III. Integrated OBC System Design

In this section, the battery pack is modeled, the OBC system is designed, and the design of the turns ratios is performed.

A. Lithium-Ion Battery Pack Modeling

Table III describes the specifications of the 40 kWh Nissan LEAF battery pack, which is selected for analysis and design purposes. These specifications were either supplied directly by the manufacturer or derived from a literature review [32]. The

$$M_C = \frac{V_2}{V_1} = \frac{\pm n\left[1 + \left(\{4\varpi - 1\}^2 + \{16\varpi + 4\}\,\kappa\, d_v + 4\,\kappa^2\{d_v^2 - 4\varphi\}\right)^{1/2} + 2\,\kappa\,\{d_v - 2\varphi\}\right]}{(1 - 2\,d_v)}. \tag{16}$$

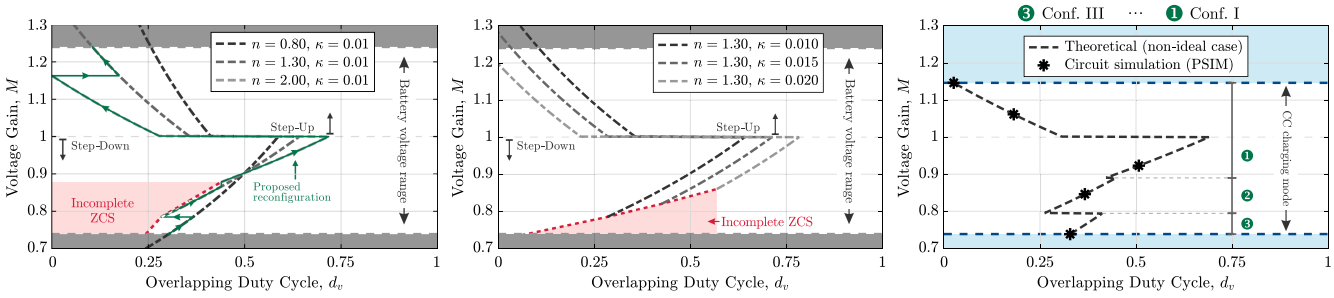

Fig. 11. Voltage gain of the S-PPC, considering only one conf. of the CFFB circuit and the proposed H-bridge reconfiguration. For different values of (a) n and (b) κ. (c) Theoretical and circuit simulation results referring to the voltage gain of the reconfigurable CFFB/OSHB S-PPC, for arbitrary values of n.

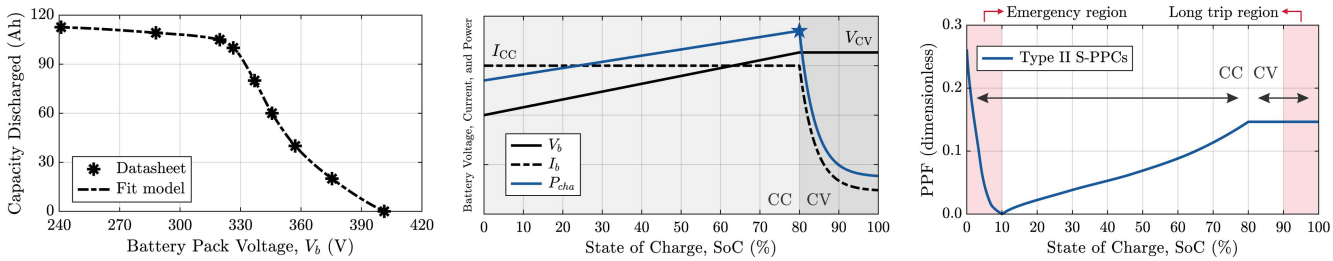

Fig. 12. (a) Modeling of the Nissan LEAF battery pack. (b) CC/CV charging profile. (c) PPF of the Type II S-PPC in the CC and CV modes.

TABLE III
NISSAN LEAF BATTERY PACK SPECIFICATIONS

Parameter	Specification
Battery type	Lithium-ion—Laminate type
Cells configuration	2 parallel strings of 96 in series
Nominal cell/pack voltage	3.65 V/350.40 V
Minimum/maximum cell voltage	2.50 V/4.20 V
Rated pack capacity/energy	112.6 Ah/40 kWh
Battery pack discharge voltage	240 – 403.20 V usable range

LEAF has two ac charging options: 1) charging at a home socket, where the 40 kWh battery pack can be charged up to 2.2 kW (Level 1), and 2) charging at a wallbox, where the battery pack can be charged up to 6.6 kW (Level 2). This EV can only be charged via the OBC from a $1-\phi$ ac grid.

Fig. 12(a) shows the capacity behavior at the beginning of life of the Nissan LEAF battery pack between the maximum and minimum voltages when discharged at 25 °C and considering a CC discharge rate [32]. Fig. 12(a) also shows the result of the battery modeling, for which the piecewise cubic Hermite interpolating polynomial of the MATLAB software is used to fit the data points extracted from the battery datasheet. For simplicity, the charge potential has been approached to the discharge potential.

Based on it, the depth of discharge (DoD) can be used to describe how deeply the batteries are discharged [33], i.e.,

$$\text{DoD} = 100\% \times \text{Available capacity} \,/\, \text{Rated capacity}. \quad (21)$$

The state of charge (SoC) of the batteries defines the energy capacity that is still available for discharge, i.e., SoC $= 100\% -$ DoD. A DoD of 100% implies that SoC $= 0\%$, so the battery pack is fully discharged and needs to be recharged [33].

B. Integrated OBC System Design

An EV battery pack must ideally be charged within a limited SoC range (e.g., 10%−90%). Continuously operating a battery pack outside the specified SoC limits is harmful to the battery lifetime [34]. If the LEAF battery pack is charged from 10% to 90% SoC, the fixed intermediate dc bus voltage can be set as equal to the battery voltage at 10% SoC. In such a case, the 10%−100% SoC range will coincide with the operation in step-up mode, while the operation in step-down mode will be restricted to an emergency (0%−10% SoC range), like if the EV is stuck in the road and needs more energy to pull over. The 90%−100% SoC range should only be used if the drivers will be taking the EV on a long road trip. Taking into account the battery model in Fig. 12(a), it is defined that $V_r \approx 325\,\text{V}$.

The battery pack is charged using the conventional CC/constant voltage (CV) charging method shown in Fig. 12(b), whose control block diagram is shown in Fig. 13 [35]. In this method, the battery pack is initially charged with a CC (I_{CC}) to prevent overcurrent conditions and later with a CV (V_{CV}), where the injected current decreases to prevent overcharging [12]. The mode transition occurs when the EV battery pack voltage reaches the voltage boundary V_{CV} [33] and the charging power is maximum [6]. In this case study, the voltage boundary for

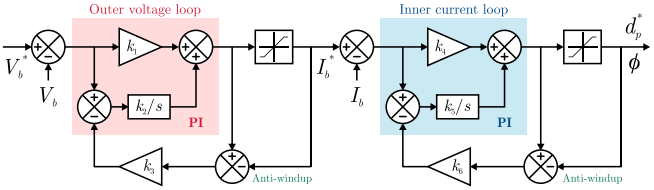

Fig. 13. Control block diagram of the CC/CV charging method.

the CV mode is set as equal to the battery pack voltage at 80% SoC [19]. It provides a safety voltage margin, ensuring that the benefits from regenerative braking can be experienced without exposing the battery pack to the risk of overvoltage. Based on the battery model in Fig. 12(a), it is obtained that $V_{\text{CV}} \approx 373\,\text{V}$.

For the proposed integrated OBC system intended for the Nissan LEAF, the total charging time can be approximated as equal to the CC charging time (t_c) [33], [36] given by

$$t_c = \Delta\text{SoC}' \times \frac{\text{Rated capacity}}{I_{\text{CC}}} \tag{22}$$

where $\Delta\text{SoC}'$ is the normalized SoC range. This approximation is valid only for lower CCs (as in Levels 1 and 2), because a larger I_{CC} shortens t_c and extends the CV charging time (t_v) [33], rendering t_v nonnegligible.

Based on it, the total charging time (t_t) for Levels 1 and 2 charging of the 40 kWh lithium-ion battery pack are

$$\begin{aligned} t_t &= 0.8 \times \frac{112.6\,\text{Ah} \times 373\,\text{V}}{2.2\,\text{kW}} \approx 19.1\,\text{h} \\ t_t &= 0.8 \times \frac{112.6\,\text{Ah} \times 373\,\text{V}}{6.6\,\text{kW}} \approx 6.40\,\text{h}. \end{aligned} \tag{23}$$

In general, a lower charging power means a lower CC I_{CC}, resulting in a slower charging process. However, lower CCs result in higher capacity utilization, higher charging efficiency, and longer battery life, reducing the total cost of the energy per cycle [33]. On the other hand, higher CCs provide a quick charge but significantly affect the aging process of the battery pack [33]. Moreover, the local distribution grid may become overloaded by fast chargers due to the high power usage during peak times [3].

C. Active Power Processing

From (3) and Fig. 12(b), it is possible to evaluate the active power actually processed by the Type II S-PPC via the figure of merit called power processing factor (PPF) [16]

$$\text{PPF} = \left|\frac{P_{\text{ind}}}{P_{\text{cha}}}\right| = \left|\frac{1}{1+M_C}\right| = |1-M| \tag{24}$$

which depends solely on the configuration and voltage gain.

Fig. 12(c) shows the PPF behavior of the proposed integrated OBC power system during the CC and CV charging modes. As illustrated, PPF $= 0$ at 10% SoC ($M = 1$), where the charging power is transferred to the battery pack without being processed by the dc–dc stage. However, the PPF of the Type II S-PPC gradually becomes more expressive when the SoC moves away from 10%. It varies from zero to 0.2616 in step-down mode (0%−10% SoC range) and from zero to 0.1465 in step-up mode (10%−100% SoC range). For $P_{\text{cha}} = 2.2\,\text{kW}$, the largest amount of active power processed by the OBC system is $|P_{\text{ind}}| \approx 371\,\text{W}$, due to the operation with PPP.

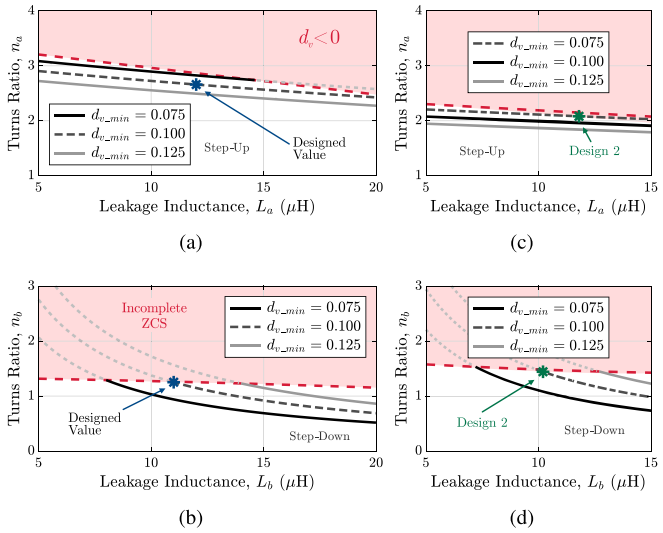

Fig. 14. Curves for the design of the turns ratios intended for the Nissan LEAF. (a) Conf. I and (b) conf. II, considering different values of L_k and d_{v_min}. (c) and (d) Curves for the design related to another model of EV.

D. Variable Transformer Turns Ratio

In summary, to obtain six possible operation ranges with confs. I–III (three in step-down mode and three in step-up mode), the following restrictions need to be satisfied:

$$n_a > n_b > n_c, \qquad n_c = (n_a n_b)/(n_a + n_b) \tag{25}$$

where n_c is the maximum value of n (in conf. III) capable of not restraining the voltage regulation range of the proposed S-PPC, given a specific EV battery pack.

One drawback of soft-switching converters is the existence of elevated circulating currents. A high circulating current implies that the nonactive power (N) processed is high in relation to the active power, i.e., a significant amount of energy that does not conduct work circulates through the converter. This circulation leads to increased conduction losses and enlarges the component ratings. In this article, the turns ratios have been designed to minimize the circulating currents [25].

Due to simplification purposes, the turns ratio for conf. I (n_a) has been designed to ensure its utilization throughout the entire VR in step-up mode. By simplifying (16) and considering the end of the CC mode ($M_C \approx -7.8$)

$$n_a \leq \frac{(2\,d_{v\_\text{min}} - 1)M_C}{(1 + |4\,\varpi - 1|)} \tag{26}$$

where d_{v_min} represents the minimum overlapping duty cycle selected by the designer to maintain $d_v > 0$ and $d_p > 0.5$.

Fig. 14(a) presents the curves for the design of the turns ratio for conf. I, considering different values of L_a and d_{v_min}. In this figure, the light red shaded area represents the inoperable regions where $d_v < 0$, and "$*$" represents the selected limit value for n_a, which is the maximum acceptable value of n_a for $L_a = 12\,\mu\text{H}$ and 2.2 kW (Level 1). Basically, to achieve a good

TABLE IV
TF COEFFICIENTS FOR THE TWO QOPS

Coefs. in (32)	Step-up / Conf. I G_{vr}^{vb}	G_{vc}^{vb}	G_{de}^{vb}	Step-down / Conf. I G_{vr}^{vb}	G_{vc}^{vb}	G_{de}^{vb}
$\alpha_1 \times 10^0$	0	0	-746	0	0	570
$\alpha_2 \times 10^6$	0	0	-2.4	0	0	2.4
$\alpha_3 \times 10^9$	0.303	0.203	-197	0.303	$+0.040$	269
$\alpha_4 \times 10^{12}$	0.005	0.007	-4.5	0.010	-0.003	7.3
$\beta_1 \times 10^0$	1	1	1	1	1	1
$\beta_2 \times 10^3$	3.2	3.2	3.2	4.2	4.2	4.2
$\beta_3 \times 10^6$	366	366	366	366	366	366
$\beta_4 \times 10^9$	7.6	7.6	7.6	9.5	9.5	9.5

TABLE V
SPECIFICATIONS OF THE CFFB/OSHB S-PPC PROTOTYPE

Parameter	Part
Dc bus (C_r) and battery (C_b) capacitors	5 μF (film)
Buffer capacitors (C_1–C_4)	27 μF (film)
Port 1 (L_1) and port 2 (L_2) inductors	660 μH and 3.2 mH
Port 1 inductor turns / core	80/2x0077867A7
Port 2 inductor turns / core	118/2x0077192A7
Switching frequency (f_s) and dead time (t_d)	50 kHz / 600 ns
Switches	UJ4C075023K4S
Transformer core	MMT520T80.50.15B
n_{p1} / n_{p2} / n_{s1} / n_{s2}	5/10/12/12
n_a, n_b, n_c	2.4, 1.2, 0.8
L_{Ma}, L_{Mb}, L_{Mc}	1.4, 5.4, and 12.4 mH
L_{k1}, L_{k2}, L_{k3}	0.6, 0.8, and 1.9 μH
L_a^*, L_b^*	11.4 and 9.8 μH
L_a, L_b, L_c	12, 10.6, and 23.1 μH

tradeoff among different factors, such as system performance and reliability, $n_a \leq 2.66$ is adopted in this case.

Complementarily, the turns ratio for conf. II (n_b) has been designed to ensure the operation at the begin of the CC charging mode ($M_C \approx +2.8$), in step-down mode. By using (9)

$$n_b \leq \frac{M_C\, d_{v\_\min}}{8\,\varpi}. \tag{27}$$

Fig. 14(b) presents the curves for the design of the turns ratio for conf. II. In this figure, the light red shaded area represents the inoperable regions where the voltage regulation is lost due to the incomplete ZCS transition, and "$*$" represents the selected limit value for n_b, which is the maximum acceptable value of n_b. In this case, $n_b \leq 1.25$ is adopted.

Based on it, the actual turns ratios and the resulting leakage inductances obtained for the realistic OBC application example are listed in Table V. These values of n and L_k guarantee ZCS turn-ON and turn-OFF for all the primary switches throughout the entire battery pack VR. In addition, by using (12) and (13) with the parameters in Table V, Fig. 15 presents the operation regions that guarantee ZVS turn-ON for all the secondary switches. Here, one can conclude that, even with variations in n and L_k, the secondary switches achieve ZVS-ON operation throughout the entire charging process.

Fig. 16 presents the root-mean-square (rms) value of the instantaneous leakage current during the CC mode, considering

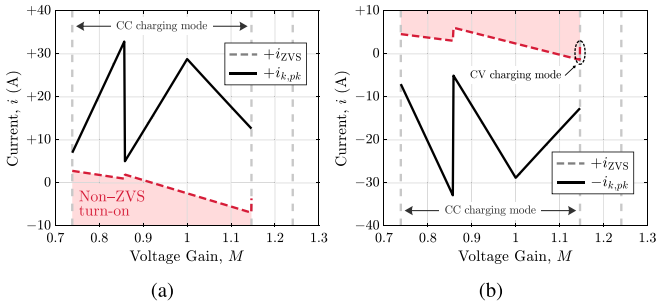

Fig. 15. ZVS-ON operation regions of the secondary switches. (a) S_5 and S_7 (where $i_{ZVS} = 2\,n\,i_{2,n}$). (b) S_6 and S_8 (where $i_{ZVS} = 2\,n\,i_{2,p}$).

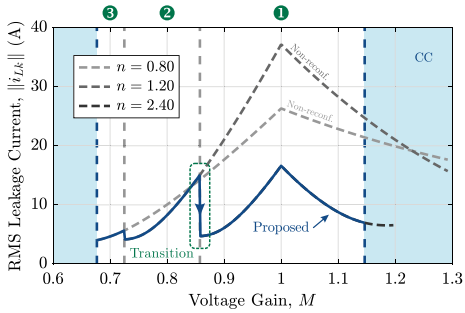

Fig. 16. Rms leakage current during the CC charging mode, with the use of a traditional nonreconfigurable H-bridge and the proposed reconfigurable H-bridge (variable turns ratio approach).

the values of n and L_k listed in Table V. Mathematically

$$\|i_{Lk}\| = \sqrt{\frac{1}{T_S}\int_0^{T_S} i_{Lk}(t)^2\,dt}\,. \tag{28}$$

In this analysis, the "$-\cdot-$" curves represent the use of a traditional nonreconfigurable H-bridge and "$-$" represents the use of the proposed reconfigurable H-bridge. In case of the nonreconfigurable S-PPC, the greater the value of n, the lower the rms leakage current (and lower the circulating currents), but the voltage gain range is narrower. Therefore, the greater the desired battery VR, the lower the required value of n and higher the circulating currents, which will lead to high conduction losses. Compared to the nonreconfigurable S-PPC, the proposed variable turns ratio approach allows the S-PPC to operate in a wide VR with low circulating currents by reconfiguring the HF transformer primary side to the optimal configuration at each operation point (OP).

The procedure for designing the turns ratios of the S-PPC intended for the LEAF is identical for any other EV model. In such a case, the design objective is always to select the values of n, L_k, and $d_{v\_\min}$ that yield a set as close as possible to the boundary of the inoperable regions, because this minimizes the circulating currents. For instance, Fig. 14(c) and (d) presents the curves for the design of the CFFB/OSHB S-PPC intended for the Tesla Model 3, where $V_{CV} \approx 398$ V. Based on the selected limits ($n_a \leq 2.08$ and $n_b \leq 1.44$), the actual values of n obtained for this second example (design 2) are $n_a = 2.00$, $n_b = 1.43$,

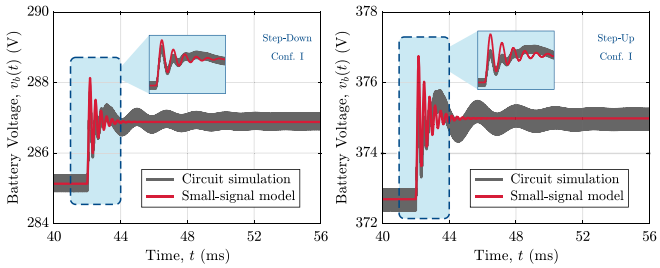

(a) (b)

Fig. 17. Behavior of the battery pack voltage in response to a step change in the ac perturbations. (a) Step-down. (b) step-up modes.

and $n_c = 0.83$. The leakage inductances are practically equal to those presented in Table V.

E. Small-Signal Modeling

In this article, the small-signal ac models of the CFFB/OSHB S-PPC have been derived utilizing the state-space averaging approach described in Erickson and Maksimović's [28] work. However, due to simplification purposes, the derivation process is omitted. Basically, the small-signal linear models are obtained by applying perturbations to the variables of interest and subsequently linearizing all the models around a given quiescent operation point (QOP). Here, the perturbed signals are expressed as

$$\langle v_r(t)\rangle_{T_S} = V_r + \hat{v}_r(t) \tag{29}$$

$$\langle v_c(t)\rangle_{T_S} = V_c + \hat{v}_c(t) \tag{30}$$

$$d_e(t) = D_e + \hat{d}_e(t) \tag{31}$$

where V_r, V_c, and D_e are the quiescent values, while $\hat{v}_r(t)$, $\hat{v}_c(t)$, and $\hat{d}_e(t)$ are the small ac perturbations [28]. In this case, (30) refers to the voltages across the buffer capacitors C_1–C_4, which have been replaced by voltage sources.

Based on it, the generalized transfer function (TF) that represents the relation between the perturbed voltage of the batteries and the ac perturbations can be expressed as

$$G_g^{vb}(s) = \frac{\hat{v}_b(s)}{\hat{g}(s)} = \frac{\alpha_1 s^3 + \alpha_2 s^2 + \alpha_3 s + \alpha_4}{\beta_1 s^3 + \beta_2 s^2 + \beta_3 s + \beta_4} \tag{32}$$

where $g = v_r$, v_c, or d_e. In consequence, $\langle \hat{v}_b(s)\rangle$ is calculated by summing the three TFs multiplied by their respective ac perturbations plus the quiescent value V_b, and the perturbed battery current is calculated by dividing $\hat{v}_b(s)$ by R_b.

Since the operation of the CFFB/OSHB S-PPC is aligned with conf. I (see Section IV-C), the models have been linearized around the following QOPs: $V_b = 285\,\text{V}$, in step-down, and $V_b = 373\,\text{V}$, in step-up mode. By considering the specifications defined later, Table IV presents the values of the TF coefficients for the two QOPs. As can be seen, the TFs for the step-down and step-up modes are different from each other; therefore, the step-up/down CFFB/OSHB S-PPC is essentially a system with two subsystems, each requiring a specific controller.

Fig. 17(a) and (b) shows the behavior of the battery pack voltage in response to a step change in the ac perturbations. In short, the errors between the simulation results and the models are due to the high-order nature of the circuit (eighth order) and the simplification of the models as third-order systems, where the dynamics imposed by L_k and C_1–C_4 are disregarded.

IV. Experimental Results and Discussions

In order to validate the analyzes, a scale-down prototype of the CFFB/OSHB S-PPC has been built to charge the LEAF battery pack up to 2.2 kW (hence, $I_{CC} = 2.2\,\text{kW}/373\,\text{V} = 5.9\,\text{A}$), emulating the Level 1 charging, which is especially appropriate for long-time or overnight charging of the EV [3]. The specifications and components used are listed in Table V. The components have been designed according to ordinary methodologies such as those found in text books [28]. For the laboratory evaluation, the lithium-ion battery pack has been emulated by a dynamic electronic load (NHR 4760).

A. Transformer Characteristics

In the prototype, the leakage inductances L_a, L_b, and L_c include the intrinsic leakage inductances of the transformer (L_{k1}, L_{k2}, and L_{k3}) and two small-sized series inductors (L_a^* and L_b^*). These small-sized inductors have been added to assist in soft-switching, and their use is necessary because the intrinsic leakage inductances are smaller than the values selected according to (26) and (27). From Table V

$$\begin{aligned} L_a &= L_{k1} + L_a^*, && \text{in Conf. I} \\ L_b &= L_{k2} + L_b^*, && \text{in Conf. II} \\ L_c &= L_{k3} + L_a^* + L_b^*, && \text{in Conf. III.} \end{aligned} \tag{33}$$

The magnetic coupling coefficients (k) [28] related to the primary and secondary windings of the HF transformer (disregarding the two series inductors) are given by

$$\begin{aligned} k_1 &= \frac{n_{sx}}{n_{p1}} \frac{L_{Ma}}{(L_{k1} + L_{Ma})\, n_a} = 0.9996, && \text{in Conf. I} \\ k_2 &= \frac{n_{sx}}{n_{p2}} \frac{L_{Mb}}{(L_{k2} + L_{Mb})\, n_b} = 0.9999, && \text{in Conf. II} \\ k_3 &= \frac{n_{sx}}{n_{pc}} \frac{L_{Mc}}{(L_{k3} + L_{Mc})\, n_c} = 0.9998, && \text{in Conf. III.} \end{aligned} \tag{34}$$

A magnetic coupling coefficient can vary between 0 and 1. In a transformer with perfect magnetic coupling, it is equal to 1, and this perfect coupling ensures maximum energy transfer between the windings, leading to an efficient power transfer within the transformer [28]. As shown in (34), the built transformer has coupling coefficients exceeding 0.9996.

B. Modulation Strategies for Soft-Switching Operation

The photograph of the experimental setup system is shown in Fig. 18. The TMS320F28335 digital controller is employed to generate the switching signals for the active switches. It is equipped with six enhanced pulse width modulator (ePWM) modules, providing twelve PWM output signals. Since the CFFB/OSHB S-PPC comprises 16 switches, an auxiliary Boolean logic circuit (BLC) has been developed to generate the 12 switching signals for the primary switches from three ePWM

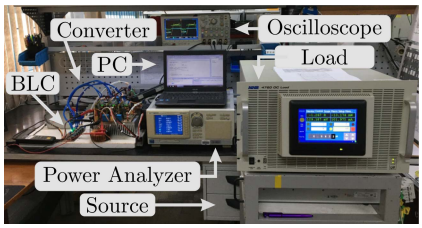

Fig. 18. Photograph of the experimental setup.

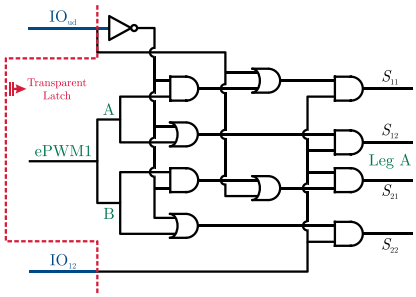

Fig. 19. Block diagram of the BLC exemplified for leg A.

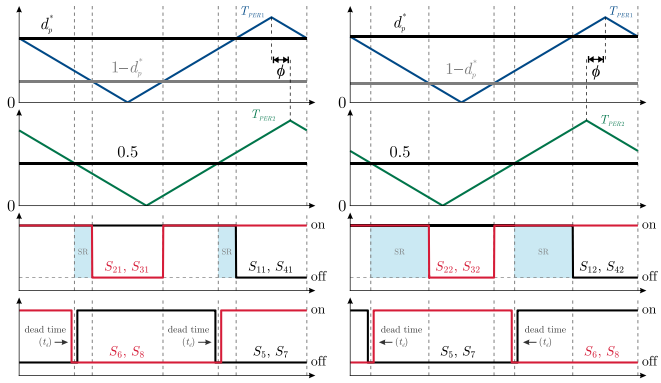

Fig. 20. PWM strategies applied to the CFFB/OSHB S-PPC in (a) step-down and (b) step-up modes (using conf. I as an example).

modules instead of six. Fig. 19 shows the block diagram of the BLC exemplified for leg A (ePWM1), where $\mathrm{IO_{ud}}$ and $\mathrm{IO_{12}}$ are the general-purpose input/output signals used to select the appropriate configuration.

Fig. 20 shows the proposed fixed-frequency PWM strategies applied to the step-up/down CFFB/OSHB S-PPC in step-down and step-up modes (using conf. I as an example). In such cases, simplifying by disregarding the dead-time intervals

$$d_p^* = (d_p + \psi) \begin{cases} \psi = 0, & \text{without SR} \\ \psi = \frac{\delta}{2}, & \text{with SR} \end{cases} \tag{35}$$

$$\phi = \left(\frac{d_v}{2} - \psi\right) 180^\circ \begin{cases} \psi = 0, & \text{without SR} \\ \psi = \frac{\delta}{2}, & \text{with SR} \end{cases} \tag{36}$$

where ϕ is the phase shift between the triangular carriers.

C. CC/CV Charging Method

Fig. 21 shows the behavior of the battery voltage, current, power (P_b), and equivalent resistance (R_b) during the charging process of the EV battery pack with the CFFB/OSHB S-PPC. In these figures, the lines correspond to the numerical simulation of the models, while the markers correspond to some data points from the experimental evaluation. In CC mode, the EV battery pack is modeled using the model presented in Section III, while in CV mode it is modeled as a simple RC equivalent circuit. Although this RC average model is not suitable to express the short term dynamic behavior of the battery pack, it is enough to represent the long term behavior.

Thus, Fig. 21 demonstrates the effectiveness of charging the LEAF battery pack within the defined VR. However, based on the values of n and L_k, the actual battery VR can indeed be divided into four segments

$$\begin{array}{ll} \text{S1: } V_b \geq V_{t3}, & \text{for VR of conf. II or III} \\ \text{S2: } V_{t2} \leq V_b < V_{t3}, & \text{for VR of conf. I} \\ \text{S3: } V_{t1} \leq V_b < V_{t2}, & \text{for VR of conf. II} \\ \text{S4: } V_b < V_{t1}, & \text{for VR of conf. III} \end{array} \tag{37}$$

where $V_{t1} \approx 236\,\mathrm{V}$, $V_{t2} \approx 279\,\mathrm{V}$, and $V_{t3} \approx 389\,\mathrm{V}$ are the threshold voltages that trigger the transitions. In this way, the operation is aligned with the S2 range, which is the one that presents the lowest rms leakage current and circulating currents, and the reconfiguration is only performed when necessary. If a different voltage boundary $V_{\mathrm{CV}} > V_{t3}$ is selected, the S-PPC can simply change its configuration to the S1 range.

In order to illustrate that the CFFB/OSHB S-PPC is able to operate in a wide VR with effective performance, Fig. 21(c) shows the values of voltage, current, power, efficiency, and voltage gain in the prototype, considering the operation in conf. II with $V_b = 485\,\mathrm{V}$ and $P_{\mathrm{cha}} = 2.2\,\mathrm{kW}$. At this OP, the system efficiency is equal to 96.23%, and the indirect power is equal to $1.08\,\mathrm{kW}$ (PPF ≈ 0.5), which occurs because P_{ind} becomes more significant when M is far from unity, increasing power losses. The limits for the VR ($219.4 - 533.4\,\mathrm{V}$ in this case) are defined by the limits of d_v and d_p^*, as well as by the expressions in (19) and (20). The VR can be extended by using a variable intermediate dc bus voltage approach [37] and/or components with higher ratings, but the S-PPC needs to be properly redesigned.

D. Converter Operation

Aiming to verify the S-PPC operation, Fig. 22 presents the experimental voltage and current waveforms measured at the HF transformer, the four-quadrant switch S_{2x} (highlighting the ZCS operation), and the two-quadrant switch S_5 (highlighting the ZVS operation). In this case, the operation is in CC charging mode (with $V_b = 285\,\mathrm{V}$), where the prototype operates with SR in step-down mode and in conf. I (S2 range).

Similarly, Fig. 23 presents the waveforms measured at the same circuit devices, but in step-up mode (with $V_b = 373\,\mathrm{V}$) and in conf. I (S2 range). As discussed in Section II, the HF oscillations observed in the voltages across the transformer primary winding and the four-quadrant switch S_{2x} are caused

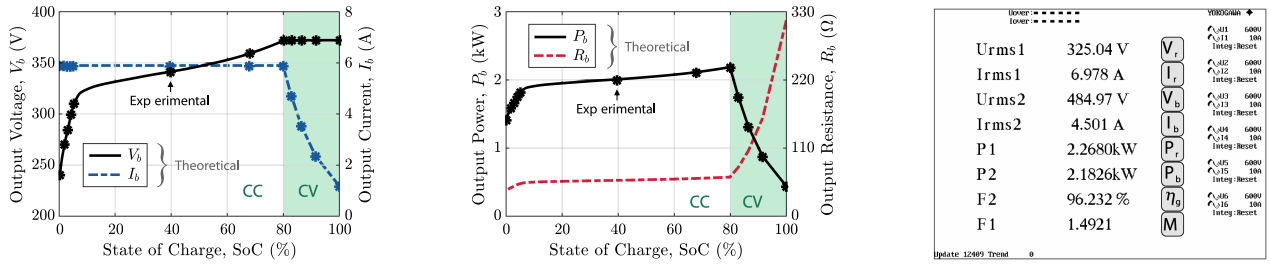

(a) (b) (c)

Fig. 21. CC/CV charging method with the CFFB/OSHB S-PPC. (a) Battery pack voltage and current. (b) Battery power and equivalent resistance. (c) Measurements of voltage, current, power, efficiency, and voltage gain in the S-PPC prototype (conf. II), for $V_b = 485\,\text{V}$ and $P_{\text{cha}} = 2.2\,\text{kW}$.

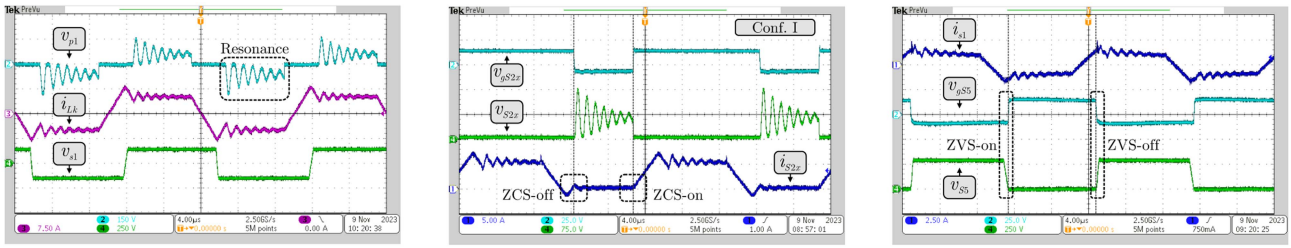

(a) (b) (c)

Fig. 22. CFFB/OSHB S-PPC experimental waveforms in step-down mode (conf. I), during the CC charging mode of the EV battery pack, where $V_b = 285\,\text{V}$. (a) At the reconfigurable transformer. (b) At the four-quadrant switch S_{2x}. (c) At the two-quadrant switch S_5.

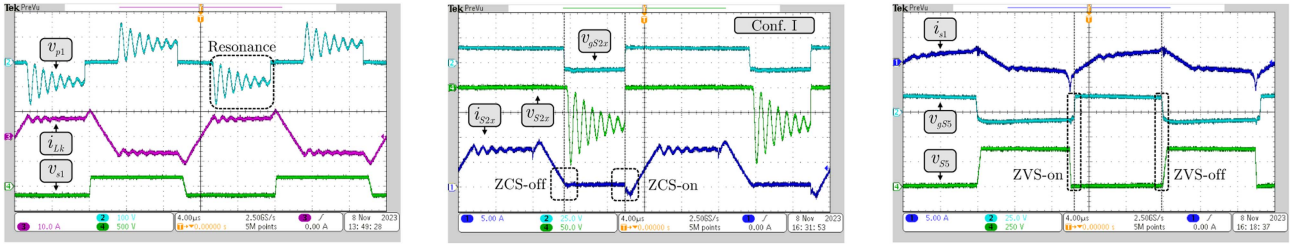

(a) (b) (c)

Fig. 23. CFFB/OSHB S-PPC experimental waveforms in step-up mode (conf. I), during the CC charging mode of the EV battery pack, where $V_b = 373\,\text{V}$. (a) At the reconfigurable transformer. (b) At the four-quadrant switch S_{2x}. (c) At the two-quadrant switch S_5.

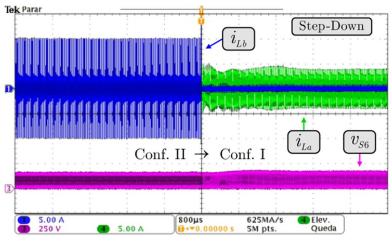

Fig. 24. Experimental waveforms of the transition from confs. II to I during the CC charging mode, in step-down mode.

by the resonance between the leakage inductance and both the parasitic capacitances of the transformer and the output capacitance of the primary switches. These voltage oscillations are quite significant because no additional snubber circuit is used, being the absence of such circuit an advantage of the proposed topology. In summary, the HF oscillations slightly increase EMI emissions and switching losses [see the additional losses highlighted in yellow in Fig. 25(b)]. Furthermore, they can indirectly increase conduction losses due to the propagation of the oscillation into the current waveforms.

The increase in EMI emissions introduced by v_{osc} is not highly significant because the major sources of EMI in power electronics circuits are the high dv/dt and di/dt involved in the switching operation of the power electronics devices [38]. Since the proposed CFFB/OSHB S-PPC operates with full-range ZCS and ZVS, where the switching transitions begin with limited dv/dt or di/dt after the turn-ON and turn-OFF moments, both the conducted and radiated EMI emissions can indeed be substantially reduced by using the proposed fixed-frequency PWM strategies that ensure soft-switching operation, even in the absence of EMI filters, enclosure, and/or shielding. Hence, this increases the reliability of the converter.

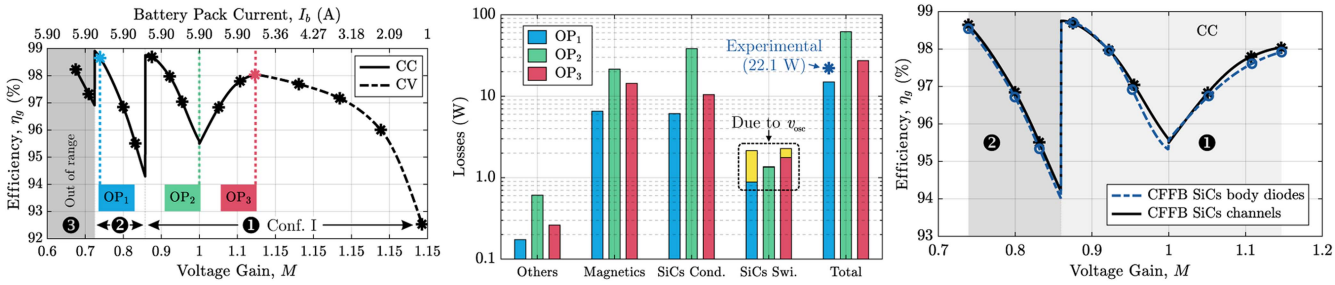

Fig. 25. Experimental results of the proposed S-PPC. (a) Overall system efficiency (η_g) during the CC and CV charging modes. (b) Analysis of the estimated power loss distribution in the S-PPC. (c) System efficiency with synchronous and non-SR during the CC charging mode.

Ignoring the voltage oscillations, the waveforms are in line with the theoretical waveforms, confirming proper operation of the S-PPC in step-down and step-up modes.

Fig. 24 shows the transition from ranges S3 to S2 during the CC charging mode, i.e., the transition from confs. II to I, with this exact point indicated in Fig. 16. In this case, the S-PPC prototype operates in step-down mode with a fixed equivalent resistance equal to $48.7\,\Omega$. In short, $i_{Lk} = i_{Lb}$ and $i_{La} = 0$ prior to the transition. Subsequent to this, however, i_{La} assumes the entire transformer current, while the n_{p2} winding is disabled. Consequently, the actual turns ratio is increased from 1.2 to 2.4, reducing both the peak and rms leakage currents (reducing the circulating currents). As can be seen, good dynamic response is achieved during the transition. Furthermore, no current and voltage spikes are generated during this moment.

E. Overall System Efficiency

Fig. 25(a) shows the overall system efficiency (η_g) of the CFFB/OSHB S-PPC with SR during the CC and CV charging modes, where "$-$" and "$-\cdot-$" denote interpolated data. Due to the previously defined specifications, the S-PPC operates only in confs. I and II in this case, but Fig. 25(a) shows the operation outside the range within which the S-PPC operates in conf. III (S4 range). The peak efficiency for the proposed S-PPC with SR is equal to 98.7% (experimental), and the minimum efficiency is equal to 92.5% (at the end of the CV mode, where $I_b = 20\%\, I_{CC}$). The peak efficiency occurs at the lower limit of the S3 range, where $P_{\text{cha}} \approx 1.68\,\text{kW}$ [see Fig. 21(b)] and, hence, the losses are approximately equal to 22 W, as shown in Fig. 25(b). The time-weighted average efficiency [39] is equal to 97%, which represents the average weight of conversion efficiency during charging.

Fig. 25(b) illustrates the estimated power loss distribution referring the reconfigurable S-PPC with SR, considering the OPs indicated in Fig. 25(a). It is evident that the primary sources of losses are the conduction losses of the switches and the copper/core losses of the magnetic devices. As anticipated, the S-PPC exhibits low switching losses. In this analysis, losses in the printed circuit board tracks and auxiliary systems are not taking into account.

Finally, Fig. 25(c) shows the system efficiency of the S-PPC with synchronous (device channel) and nonsynchronous (body diode) rectification, during the CC charging mode. As can be seen, both approaches exhibit similar performance, with the SR yielding slightly higher overall system efficiency.

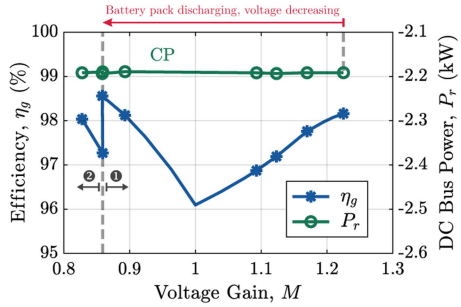

Fig. 26. Overall efficiency and system active power during the CP discharging mode, considering the sets of n and L_k corresponding to design 2.

F. Discharging Mode

To validate the flexibility of the proposed integrated OBC system, Fig. 26 shows the overall efficiency and system active power during the constant power (CP) discharging mode of the EV battery pack, considering the three sets of turns ratios and tuned leakage inductances corresponding to the design of the CFFB/OSHB S-PPC intended for the Tesla Model 3 (design 2 in Section III-D). Since the forward conduction direction during charging has been defined as the positive value, the constant discharging power is negative ($-2.2\,\text{kW}$) and flows from the battery pack to the dc bus. In this case, the peak efficiency is equal to 98.6%, and the minimum efficiency is equal to 96.1%, indicating that the CFFB/OSHB S-PPC is efficient in both charging and discharging the batteries. The capacity to operate with bidirectional active power flow enables the proposed integrated OBC system to facilitate vehicle-to-grid, vehicle-to-home, vehicle-to-load, and vehicle-to-vehicle functionalities, which are a trend in the EV market and can be very useful for users [40].

G. Comparative Evaluation

Table VI demonstrates a comprehensive comparison between the CFFB/OSHB S-PPC and some reconfigurable full power converters published in the literature for EV applications, which have been applied to OBCs [9], [13], [15] and FCSs [41]. They

TABLE VI
COMPARISON BETWEEN THE CFFB/OSHB S-PPC AND SOME RECONFIGURABLE CONVERTERS FOR EV CHARGING APPLICATIONS

Parameter	[15] 2018	[9] 2021	[41] 2023	[13] 2023	Proposed
Topology	LLC resonant	LLC resonant	Semi-DAB	Multi-resonant	CFFB/OSHB S-PPC
Dc bus and battery terminals	VF and VF	VF and VF	VF and VF	VF and VF	CF and CF
Modulation	PWM + Phase shift	Singular frequency	Phase shift + PWM	Pulse frequency	PWM + Phase shift
Reconfiguration	Voltage rectifier	Turns ratio/H-bridge	Turns ratio/H-bridge	Resonant tank	Turns ratio
Possible confs.	3	4	4	3	3
Switches (S) + diodes (D)	$5S+6D$	$8S+6D$	$10S+2D$	$12S$	$16S$
Max. number of HF switches	$5S$	$4S$	$6S$	$8S$	$8S$
Transformers (T)	$1T$ (two windings)	$1T$ (three windings)	$1T$ (three windings)	$1T$ (two windings)	$1T$ (four windings)
Soft-switching	ZVS/ZCS	ZVS/ZCS	ZVS/ZCS	ZVS/ZCS	ZCS/ZVS
Active power flow capability	Unidirectional	Unidirectional	Unidirectional	Bidirectional	Bidirectional
Active power processed	Full	Full	Full	Full	Partial
Dc bus voltage	390 V	390 V	$350-550$ V	400 V	325 V
Battery voltage	$250-420$ V	$60-450$ V	$150-450$ V	$160-400$ V	$219-533$ V
Switching frequency	100 kHz	<250 kHz	100 kHz	$80-180$ kHz	50 kHz
Power level (P_L)	1.3 kW	1.8 kW	10 kW	1 kW	2.2 kW
σ (\$/W)	0.0261	0.0594	0.0745	0.1162	0.0549
Peak efficiency	93.94%	97.50%	98.50%	93.00%	98.7%
Wide-load-range efficiency	$\approx 84\%$	$<90\%$	$\approx 94\%$	$<87\%$	92.5%

are compared based on the topology and modulation strategy, reconfigurable parameter, number of confs., number of semiconductors and transformer windings, soft-switching characteristics, active power behavior, voltages and power levels, switching frequency, and system efficiency. In addition, the following relative cost-effectiveness factor (σ) is employed to compare the cost of the semiconductors (as they are typically the most expensive parts of a converter)

$$\sigma[\$/\mathrm{W}] = \frac{(c_s S + c_d D)}{P_L F} \tag{38}$$

where c_s and c_d are the cost per unit of the switches and diodes, respectively, and F is a factor equal to 1 for unidirectional converters and 2 for bidirectional converters, indicating that the bidirectional active power flow capability results in a low factor, which is advantageous. For this analysis, the costs per unit have been obtained from DigiKey on 15 May 2024.

In summary, some of the most commonly used reconfigurable topologies for the 400 V EV charging applications are based on resonant [9], [13], [15] and dual-active-bridge (DAB) converters [41], which can reconfigure the secondary side rectifier, the resonant tank, or both the turns ratio and primary side inverter. In such cases, while the converters in [15] and [41] operate with a fixed switching frequency, such as the CFFB/OSHB S-PPC, those in [9] and [13] operate with variable frequency, increasing the control implementation complexity [24]. All the evaluated topologies (including the CFFB/OSHB S-PPC) present three or four possible confs., employ a single HF transformer with two or more windings, and achieve soft-switching operation. However, it is noteworthy that only the proposed CFFB/OSHB S-PPC performs PPP and presents nonpulsating current with low ripple on both sides of the dc–dc stage. In addition, only it and the converter in Reddy and Das's [13] work are bidirectional.

The CFFB/OSHB S-PPC presents a higher peak efficiency than all the converters in Table VI, and a higher wide-load-range efficiency than all those applied to OBCs [9], [13], [15]. The converter in Rafi and Bauman's [41] work presents a higher wide-load-range efficiency of approximately 94%; however, only the CC mode has been evaluated by the authors, with a minimum power of 3.75 kW (due to its application in an FCS). On the other hand, it can be seen that Shang and Wang [15] employed the most cost-effective semiconductors (0.0261\$/W), despite being unidirectional. Meanwhile, the converters in [13] and [41] are the least cost-effective, and the converter in Shu and Wang's [9] work exhibits middling cost-effectiveness similar to the CFFB/OSHB S-PPC. Therefore, although the number of semiconductors in the proposed S-PPC is slightly higher than in the other converters, 1) its efficiencies are notably high, and 2) the relative cost of the semiconductors is acceptable.

In short, there are two ways to reduce the semiconductor count in the S-PPC to a minimum of *eight* discrete devices. First, the use of 1200-V switches enables the utilization of only one half-bridge cell at port 2, i.e., only two switches. The second way involves the use of monolithic bidirectional (MBD) instead of back-to-back switches in the CFFB equivalent circuit. In this technology, dual-gate ac switches are monolithically integrated into a single chip on the wafer, thereby simplifying packaging and enhancing performance. Unfortunately, however, the MBD switches are not commercially available yet [42].

Finally, Table VII presents a brief comparison between the proposed S-PPC and some available S-PPCs applied to OBCs [18] and FCSs [14], [43]. In Rivera et al.'s [14] work, the step-up/down three-port PSFB S-PPC employs 16 semiconductor devices ($8S+8D$) and it can be reconfigured as either Type I or Type II [14]. Although it can operate in a wide battery VR, the authors have not provided experimental results to validate the proposed approach. Moreover, unlike the CFFB/OSHB S-PPC, it is unidirectional and capable of achieving only ZVS operation. In Pesantez et al.'s [43] work, the transformerless PSFB Type I S-PPC is unidirectional, nonreconfigurable, and operates at a very low switching frequency of 10kHz. Despite the moderate number of semiconductors in such a step-up S-PPC ($4S+4D$) [43], its operation is constrained to a narrow VR (75 V in that article), which is inadequate for EV charging

TABLE VII
COMPARISON BETWEEN THE CFFB/OSHB S-PPC AND SOME S-PPCS FOR EV CHARGING APPLICATIONS

Parameter	[14] 2021	[43] 2023	[18] 2024	Proposed
S-PPC	Three-port	PSFB	DAB	CFFB/OSHB
Type	I & II	I	II	II
Reconfigurable	Yes	No	No	Yes
Switches (S) + diodes (D)	$8S + 8D$	$4S + 4D$	$8S$	$16S$
Functional isolation	Transformer	Capacitive	Transformer	Transformer
Active power flow capability	Unidirectional	Unidirectional	Bidirectional	Bidirectional
Soft-switching	ZVS	–	ZVS	ZCS/ZVS
Voltage gain capability	Step-up/down	Step-up	Step-down	Step-up/down
Battery VR (ΔV_b)	510 V	75 V	75 V	314 V
Switching frequency	150 kHz	10 kHz	40 kHz	50 kHz
Power level	$12 - 24$ kW	1.6 kW	3 kW	2.2 kW
Peak efficiency (exp.)	–	95.35%	$> 99\%$	98.7%
Wide-load-range efficiency (exp.)	–	$\approx 91\%$	$< 98\%$	92.5%

applications. Nevertheless, it presents peak and wide-load-range efficiencies lower than those of the CFFB/OSHB S-PPC, even operating at a similar power level. The step-down DAB Type II S-PPC in Anzola et al.'s [18] work presents efficiencies higher than those of the CFFB/OSHB S-PPC; however, only the CC mode has been evaluated by the authors. Moreover, despite its bidirectional power flow capability and the moderate number of switches it employs ($8S$), its ZVS range is limited and its operation is also constrained to a narrow VR of 75 V [18].

As can be seen, therefore, there exists a lack of researching around bidirectional reconfigurable S-PPCs applied to wide step-up/down VR integrated OBCs, which is where the proposed snubberless CFFB/OSHB Type II S-PPC with full-range soft-switching operation takes place.

V. CONCLUSION

This article proposed a step-up/down Type II S-PPC with a reconfigurable H-bridge for the dc–dc stage of an integrated OBC. The proposed CFFB/OSHB S-PPC performs PPP and can reconfigure its primary side with three sets of turns ratios and leakage inductances, which have been designed to reduce the conversion effort by minimizing the circulating currents. In consequence, the variable turns ratio approach allows the S-PPC to operate in a wide battery VR with high performance. Moreover, full-range ZCS is achieved for all the primary switches and ZVS for all the secondary switches, which have been ensured by two fixed-frequency PWM strategies. They also realize the high-voltage spike suppression of the primary switches without any additional circuit. The proposed S-PPC is also bidirectional, presents nonpulsating current with low ripple on both sides of the dc–dc stage, and does not require relays or contactors for reconfiguration.

To validate the proposal, a scale-down laboratory prototype has been built to charge an EV battery pack up to 2.2 kW (Level 1 charging). In short, the prototype achieved a peak system efficiency of 98.7% and a wide-load-range efficiency of 92.5%. Experimental results corresponding to design 2 have also demonstrated that the step-up/down CFFB/OSHB S-PPC is efficient in both charging and discharging the batteries.

REFERENCES

[1] M. Yilmaz and P. T. Krein, "Review of battery charger topologies, charging power levels, and infrastructure for plug-in electric and hybrid vehicles," *IEEE Trans. Power Electron.*, vol. 28, no. 5, pp. 2151–2169, May 2013.

[2] H. Li, Z. Zhang, S. Wang, J. Tang, X. Ren, and Q. Chen, "A 300-kHz 6.6-kW SiC bidirectional onboard charger," *IEEE Trans. Ind. Electron.*, vol. 67, no. 2, pp. 1435–1445, Feb. 2020.

[3] S. S. G. Acharige, M. E. Haque, M. T. Arif, N. Hosseinzadeh, K. N. Hasan, and A. M. T. Oo, "Review of electric vehicle charging technologies, standards, architectures, and converter configurations," *IEEE Access*, vol. 11, pp. 41218–41255, Apr. 2023.

[4] F. Blaabjerg, H. Wang, I. Vernica, B. Liu, and P. Davari, "Reliability of power electronic systems for EV/HEV applications," *Proc. IEEE*, vol. 109, no. 6, pp. 1060–1076, Jun. 2021.

[5] J.-H. Choi, H.-M. Kwon, and J.-Y. Lee, "Design of a 3.3 kW/100 kHz EV charger based on flyback converter with active snubber," *IEEE Trans. Veh. Technol.*, vol. 71, no. 7, pp. 7161–7170, Jul. 2022.

[6] C.-Y. Lim, Y. Jeong, and G.-W. Moon, "Phase-shifted full-bridge DC–DC converter with high efficiency and high power density using center-tapped clamp circuit for battery charging in electric vehicles," *IEEE Trans. Power Electron.*, vol. 34, no. 11, pp. 10945–10959, Nov. 2019.

[7] J.-W. Kim and P. Barbosa, "PWM-controlled series resonant converter for universal electric vehicle charger," *IEEE Trans. Power Electron.*, vol. 36, no. 12, pp. 13578–13588, Dec. 2021.

[8] H. Wang, M. Shang, and D. Shu, "Design considerations of efficiency enhanced PEV charger using reconfigurable transformer," *IEEE Trans. Veh. Technol.*, vol. 68, no. 9, pp. 8642–8651, Sep. 2019.

[9] D. Shu and H. Wang, "An ultrawide output range LLC resonant converter based on adjustable turns ratio transformer and reconfigurable bridge," *IEEE Trans. Ind. Electron.*, vol. 68, no. 8, pp. 7115–7124, Aug. 2021.

[10] B.-R. Lin, "Analysis and implementation of a frequency control DC–DC converter for light electric vehicle applications," *Electronics*, vol. 10, no. 14, Jul. 2021, Art. no. 1623.

[11] M. I. Shahzad, S. Iqbal, and S. Taib, "A wide output range HB-2LLC resonant converter with hybrid rectifier for PEV battery charging," *IEEE Trans. Transport. Electrific.*, vol. 3, no. 2, pp. 520–531, Jun. 2017.

[12] Y.-J. Choi et al., "A high efficiency LLC resonant converter-based li-ion battery charger with adaptive turn ratio variable scheme," *J. Elect. Eng. Technol.*, vol. 13, no. 1, pp. 124–132, Jan. 2018.

[13] R. Reddy and M. Das, "A reconfigurable bidirectional DC–DC converter with integrated battery heating for electric vehicle applications," *IEEE Trans. Emerg. Sel. Topics Ind. Electron.*, vol. 4, no. 4, pp. 1181–1191, Oct. 2023.

[14] S. Rivera, F. Flores-Bahamonde, H. Renaudineau, T. Dragicevic, and S. Kouro, "A buck–boost series partial power converter using a three-port structure for electric vehicle charging stations," in *Proc. 2021 IEEE Energy Convers. Congr. Expo. (ECCE)*, 2021, pp. 1749–1754.

[15] M. Shang and H. Wang, "A voltage quadrupler rectifier based pulsewidth modulated LLC converter with wide output range," *IEEE Trans. Ind. Appl.*, vol. 54, no. 6, pp. 6159–6168, Nov./Dec. 2018.

[16] N. G. F. dos Santos, J. R. R. Zientarski, and M. L. d. S. Martins, "A review of series-connected partial power converters for DC–DC applications," *IEEE Trans. Emerg. Sel. Topics Power Electron.*, vol. 10, no. 6, pp. 7825–7838, Dec. 2022.

[17] J. Anzola et al., "Review of architectures based on partial power processing for DC–DC applications," *IEEE Access*, vol. 8, pp. 103405–103418, 2020.
[18] J. Anzola, S. harma, I. Aizpuru, S. Bhattacharya, and J. S. Artal-Sevil, "Performance improvement of a silicon partial power converter over a silicon carbide full power converter," *IEEE Trans. Transport. Electrific.*, vol. 10, no. 1, pp. 1680–1691, Mar. 2024.
[19] V. M. Iyer, S. Gulur, G. Gohil, and S. Bhattacharya, "An approach towards extreme fast charging station power delivery for electric vehicles with partial power processing," *IEEE Trans. Ind. Electron.*, vol. 67, no. 10, pp. 8076–8087, Oct. 2020.
[20] S. Rivera et al., "Partial-power converter topology of type II for efficient electric vehicle fast charging," *IEEE Trans. Emerg. Sel. Topics Power Electron.*, vol. 10, no. 6, pp. 7839–7848, Dec. 2022.
[21] Y. Zhang et al., "A dual-current-fed dual-active-bridge dc/dc converter with high-frequency current-ripple-friendly ports," *IEEE Trans. Power Electron.*, vol. 37, no. 12, pp. 15084–15098, Dec. 2022.
[22] L. Zhu, "A novel soft-commutating isolated boost full-bridge ZVS-PWM DC–DC converter for bidirectional high power applications," *IEEE Trans. Power Electron.*, vol. 21, no. 2, pp. 422–429, Mar. 2006.
[23] T. -F. Wu, J. -G. Yang, C. -L. Kuo, and Y. -C. Wu, "Soft-switching bidirectional isolated full-bridge converter with active and passive snubbers," *IEEE Trans. Ind. Electron.*, vol. 61, no. 3, pp. 1368–1376, Mar. 2014.
[24] P. Xuewei and A. K. Rathore, "Naturally clamped zero-current commutated soft-switching current-fed push–pull dc/dc converter: Analysis, design, and experimental results," *IEEE Trans. Power Electron.*, vol. 30, no. 3, pp. 1318–1327, Mar. 2015.
[25] P. Xuewei and A. K. Rathore, "Novel bidirectional snubberless naturally commutated soft-switching current-fed full-bridge isolated DC/DC converter for fuel cell vehicles," *IEEE Trans. Ind. Electron.*, vol. 61, no. 5, pp. 2307–2315, May 2014.
[26] K.-H. Liu and F. C. Lee, "Topological constraints on basic PWM converters," in *Proc. 19th Annu. IEEE Power Electron. Spec. Conf. (PESC)*, Apr. 1988, pp. 164–172.
[27] D.-H. Kim, M.-J. Kim, and B.-K. Lee, "An integrated battery charger with high power density and efficiency for electric vehicles," *IEEE Trans. Power Electron.*, vol. 32, no. 6, pp. 4553–4565, Jun. 2017.
[28] R. W. Erickson and D. Maksimović, *Fundamentals of Power Electronics*, 2nd ed., Alphen aan den Rijn, The Netherlands: Kluwer, 2004.
[29] T. J. Liang and J.-H. Lee, "Novel high-conversion-ratio high-efficiency isolated bidirectional DC–DC converter," *IEEE Trans. Ind. Electron.*, vol. 62, no. 7, pp. 4492–4503, Jul. 2015.
[30] X.-F. Cheng, C. Liu, D. Wang, and Y. Zhang, "State-of-the-art review on soft-switching technologies for non-isolated DC–DC converters," *IEEE Access*, vol. 9, pp. 119235–119249, 2021.
[31] B. Han, C. Bai, J. S. Lee, and M. Kim, "Repetitive controller of capacitorless current-fed dual-half-bridge converter for grid-connected fuel cell system," *IEEE Trans. Ind. Electron.*, vol. 65, no. 10, pp. 7841–7855, Oct. 2018.
[32] "Nissan LEAF 40-kWh battery: Deep dive, InsideEVs," 2018. [Online]. Available: https://insideevs.com
[33] A. Bocca, Y. Chen, A. Macii, E. Macii, and M. Poncino, "Aging and cost optimal residential charging for plug-in EVs," *IEEE Des. Test*, vol. 35, no. 6, pp. 16–24, Dec. 2018.
[34] M. A. Hannan, M. M. Hoque, A. Hussain, Y. Yusof, and P. J. Ker, "State-of-the-art and energy management system of lithium-ion batteries in electric vehicle applications: Issues and recommendations," *IEEE Access*, vol. 6, pp. 19362–19378, 2018.
[35] M. C. Kisacikoglu, M. Kesler, and L. M. Tolbert, "Single-phase on-board bidirectional PEV charger for V2G reactive power operation," *IEEE Trans. Smart Grid*, vol. 6, no. 2, pp. 767–775, Mar. 2015.
[36] F. Faanzir, M. Ashari, S. Soedibyo, and U. Umar, "Determining the shortest charging time of batteries using SOC set point at constant current–constant voltage mode," *Przeglad Elektrotechniczny*, vol. 97, no. 4, pp. 54–59, 2021.
[37] S. Zhao, A. Kempitiya, W. T. Chou, V. Palija, and C. Bonfiglio, "Variable DC-link voltage LLC resonant dc/dc converter with wide bandgap power devices," *IEEE Trans. Ind. Appl.*, vol. 58, no. 3, pp. 2965–2977, May/Jun. 2022.
[38] H. Chung, S. Y. R. Hui, and K. K. Tse, "Reduction of power converter EMI emission using soft-switching technique," *IEEE Trans. Electromagn. Compat.*, vol. 40, no. 3, pp. 282–287, Aug. 1998.
[39] Z. Fang, T. Cai, S. Duan, and C. Chen, "Optimal design methodology for LLC resonant converter in battery charging applications based on time-weighted average efficiency," *IEEE Trans. Power Electron.*, vol. 30, no. 10, pp. 5469–5483, Oct. 2015.
[40] S. Wang et al., "Multifunction capability of SiC bidirectional portable chargers for electric vehicles," *IEEE Trans. Emerg. Sel. Topics Power Electron.*, vol. 9, no. 5, pp. 6184–6195, Oct. 2021.
[41] M. A. H. Rafi and J. Bauman, "High-efficiency variable turns-ratio semi-dual active bridge converter for a DC fast charging station with energy storage," *IEEE Trans. Transport. Electrific.*, vol. 9, no. 3, pp. 3918–3935, Sep. 2023.
[42] V. Veliadis, "Monolithic bidirectional WBG switches rekindle power electronics technology [expert view]," *IEEE Power Electron. Mag.*, vol. 10, no. 1, pp. 71–75, Mar. 2023.
[43] D. Pesantez, H. Renaudineau, S. Rivera, A. Peralta, A. Marquez Alcaide, and S. Kouro, "Transformerless partial power converter topology for electric vehicle fast charge," *IET Power Electron.*, vol. 17, no. 8, pp. 970–982, 2023.

Niwton Gabriel Feliciani dos Santos was born in Rosário do Sul, Brazil, in 1995. He received the B.S. degree (Hons.) from the Federal University of Pampa, Alegrete, Brazil, in 2018, and the M.S. degree from the Federal University of Santa Maria, Santa Maria, Brazil, in 2020, both in electrical engineering. He is currently working toward the Ph.D. degree in electrical engineering with the Federal University of Santa Maria.

His research interests include active and nonactive power processing, partial power converters, battery chargers for electric vehicles, and photovoltaic systems.

Jonatan Rafael Rakoski Zientarski (Member, IEEE) was born in Ijuí, Brazil, in 1983. He received the B.S. degree in electrical engineering from the Regional University of Northwest Rio Grande do Sul State, Ijuí, Brazil, in 2006, and the M.S. and Ph.D. degrees in electrical engineering from the Federal University of Santa Maria, Santa Maria, Brazil, in 2009 and 2017, respectively.

Since 2010, he has been a Professor with the Catarinense Federal Institute of Education, Science, and Technology, Videira, Brazil. His research interests include modeling, design, and optimization of power converters, as well as renewable energy applications.

Mário Lúcio da Silva Martins (Member, IEEE) received the B.S., M.S., and Ph.D. degrees in electrical engineering from the Federal University of Santa Maria, Santa Maria, Brazil, in 1999, 2002, and 2008, respectively.

From 2006 to 2012, he was with the Federal University of Technology–Paraná, Pato Branco, Brazil. In 2012, he joined the Department of Electronics and Computation, Federal University of Santa Maria. His research interests include high-voltage gain converters, partial power converters, electric vehicles, and power converters for renewable energy.